HYDRODYNAMIC CALCULATIONS ON SOLID AND LIQUID TARGETS

T.W. Eaton and A. Poncet

This note describes some hydrodynamic calculations of shock waves transients resulting from sudden beam energy deposition into possible $\bar{p}$ production targets, using the computer code REXCO[1].

1. INTRODUCTION

The REXCO program assumes that target materials may be treated as liquid, solid, elastic plastic and that the cases considered have axial symmetry in that there is no motion in the circumferential θ direction and no variables of the system depend upon θ. In the numerical analysis of the effect of a sudden input of energy to the system, all flow equations (mass, momentum, energy) are expressed in moving (Lagrangian) material co-ordinates and then set into numerical form by finite difference equations. For each problem, the code computes the accelerations, velocities, displacements, volume changes, densities, stresses, pressures and energies at every spatial point for a specific time interval. For elastic plastic materials, such as the containing vessel, the code also calculates the membrane stresses, both axial and angular.

Initially the REXCO code was used to analyse the case of a simple mercury column enclosed in a stainless steel closed cylinder. Although this example is of little practical use, since no insulating ceramic layer was included, the results are informative and will therefore be discussed fully before going on to more practical cases.

2. MERCURY COLUMN IN STAINLESS STEEL VESSEL OF WALL THICKNESS 0.5 mm

REXCO calculations assume symmetry about a central axis and in the first example, the mercury column was considered as being divided into fifteen radial zones, each of width 0.1 mm, and twenty axial zones, of length 0.25 mm. This makes up a mercury column of radius 1.5 mm and length 50 mm, which is about half the optimum length for antiproton production. In all cases, therefore, the total absorbed energy (E_0) was taken as half that assumed to be absorbed in a real target. Initially E_0 was taken as 5×10^8 dynes.cm.gm^{-1} and, in later runs of the programme, was increased to 5×10^9 dynes.cm.gm^{-1}. These energies correspond respectively to 160 and 1600 Joules absorbed in the target, and were assumed to be absorbed in the first five radial zones, of the fifteen available.

Figures 1a and 1b show the variation of radial zone pressure as a function of time from energy input. No capability existed within the programme to spread the deposition of energy over the known pulse time of 500 ns, the whole of E_0 being therefore deposited at $t = 0$. It will be clearly seen that a shock wave propagates from the input zones towards the cylinder wall at a constant speed. The position of the shock wave as a function of time, is given in Table 1 and plotted in Fig. 2a. The gradient of this graph gives the velocity of shock wave

propagation in mercury namely $(2.4 \pm 0.1) \times 10^3$ ms^{-1}, and agrees with experimental results of other workers[2]. It is also of interest to note that a significant reflection of the shock wave occurs after a time ~500 ns when the pressure wave reaches radial zone 16, the location of the stainless steel shell and could provide a means of self pumping in a liquid target.

The pressure variation in zone 2 as a function of time from energy input is shown in Fig. 2b and clearly shows the oscillatory dependence, even down to the very rapid oscillation which occurred at the times of maximum pressure when two shock waves, reflected from opposite vessel walls, met at the centre of the mercury column.

The density of the mercury column suffers only small decreases in the inner radial zones, when subjected to the lower input energy of 160 J, as shown in Fig. 3a. The decrease becomes much more significant for 1600 J input, as shown in Fig. 3b, but in both cases it will be observed that the density, at any particular inner radial zone, is oscillatory in nature, returning eventually to the normal state. This is contrary to the behaviour found in Cu targets to be discussed later.

The angular and axial stresses in the stainless steel vessel only become significant after a time of 450 ns, which is in accord with the observations of shock wave propagation, discussed previously. All stresses and strains show a characteristic maximum at t = 1000 ns, furthermore reverse from tensile to compressive and finally back to tensile as the vessel oscillates about its natural equilibrium state, as shown in Fig. 4a). This behaviour is perfectly shown in the computer print out of the radial displacement at mesh point 16, the position of the stainless steel vessel, given in Fig. 4b.It will be observed that the peaks of Fig. 4b occur at the same time as the peak tensile stresses of Fig. 4a and the trough coincide with the smaller compressive peaks.

$$\left.\begin{aligned} &\text{Angular Strain} = 1.5 \times 10^{-2} \\ &\text{Angular Stress} = 2.4 \times 10^{9} \text{ dynes cm}^{-2} \ [0.35 \times 10^{5} \text{ Psi}] \\ &\text{Axial Stress} = 7.8 \times 10^{8} \text{ dynes cm}^{-2} \ [1.1 \times 10^{4} \text{ Psi}] \end{aligned}\right\} \ Y$$

These stresses and strains are below the quasi static values one could expect from the initial pressure increase. This behaviour, however, is expected if the elastic response time of the stainless steel vessel is long compared to the time of the pressure wave. Indeed, elastic waves are propagating much more slowly than hydrodynamic high pressure waves.

Decreasing the energy input to 160 J decreases the maximum vessel stresses and strains to new peak values of:

$$\left.\begin{aligned} &\text{Angular Strain} = 2.6 \times 10^{-3} \\ &\text{Angular Stress} = 4.4 \times 10^{8} \text{ dynes cm}^{-2} \ [0.64 \times 10^{4} \text{ Psi}] \\ &\text{Axial Stress} = 1.3 \times 10^{8} \text{ dynes cm}^{-2} \ [0.2 \times 10^{4} \text{ Psi}] \\ &\text{Axial Strain} \rightarrow 0 \end{aligned}\right\} \ X$$

These stresses are respectively equivalent to pressures of 435 × and 136 × atmospheres.

All of these values are well within the capability of stainless steel as a containing vessel, assuming a yield strength of 10^{10} dynes cm^{-2}.

3.

3.1 Mercury Column Enclosed in Thin Ceramic Sheath, Inside Stainless Steel Vessel 5 mm Thickness

The input data to the REXCO programme was changed to include a ceramic insulator (Sapphire) located in the last seven radial zones of the fifteen available. The dimensions of the mercury and ceramic, in the first few runs, were as shown below and although it is clear that the ceramic thickness is far smaller than used in practice, the results, however, showed some interesting features.

$$[r_{Hg} = 0.8 \text{ mm. Outer radius of ceramic} = 1.5 \text{ mm}] .$$

a) The density variation in the mercury was oscillating in nature as before, but in this case showed clearly the region of reduced density, in which the deposition of energy took place, and a region of enhanced density, up to the wall of the ceramic liner, as shown in Fig. 5.

b) The stainless steel vessel was now partially shielded from the effects of the energy, inputed into the mercury, by the ceramic insert. Up to a time of 1500 ns the vessel stresses and strains gradually increase asymptotically up to maximum values, quoted below, which are much less than the values quoted for a simple mercury column with the same energy input (data Y). These variations are shown in Fig. 6, and were all tensile, the normal oscillatory behaviour being damped by shock wave reflection at, and absorbtion in the ceramic sheath.

$$\left.\begin{array}{lcl} \text{Angular Strain} & = & 1.4 \times 10^{-3} \\ \text{Angular Stress} & = & 2.2 \times 10^{8} \text{ dynes cm}^{-2} \ [0.32 \times 10^{4} \text{ Psi}] \\ \text{Axial Stress} & = & 6.7 \times 10^{7} \text{ dynes cm}^{-2} \ [1.0 \times 10^{4} \text{ Psi}] \end{array}\right\} Z$$

These results suggest that the ceramic must be suffering detrimental effects and this view is supported by Fig. 7 which shows the radial strain in the ceramic across its thickness. It is clearly seen that these values are far in excess of what the ceramic could withstand over many cycles.

The next step in the procedure therefore was to increase the outer ceramic radius to 51 mm in line with the dimensions of the ceramic used in the present copper targets.

3.2 Mercury Column Enclosed in Thick Ceramic Sheath, Inside Stainless Steel Vessel of Thickness 5 mm

$E_0 = 2.5 \times 10^{9}$ dynes cm gm^{-1}, equivalent to 800 J.

The radial dependence of the density of the mercury target, in this case behaved very similarly to the case of a thin ceramic, shown in Fig. 5, the largest decrease in central zone density being 18% after a time of 1250 ns after energy deposition.

The vessel stresses and strains are shown in Fig. 8 a) and reflect the enhanced effect of the greater thickness of ceramic. It is of interest to note that, although the general shape of the distributions is similar to those shown in Fig. 6, they are all shifted to far higher times from energy input, reflecting the effect of the thick ceramic layer. All are within tolerable limits. The appearance of vessel stresses and strains at a time of 4000 ns is supported by the computer output of radial displacement at zone 16, shown in Fig. 8b) together with the pressure variation in the inner mercury zone 2.

The radial strain in the ceramic is shown in Fig. 9 and shows that, whilst high values still do occur, they are confined to the first two inner radial zones and that there is a rapid drop in strain towards the outer zones, not found in the case of a thin ceramic, shown in Fig. 7. Furthermore, there is a much clearer dependence on time, reaching an average maximum value at about 2000 ns and decreasing thereafter. The ceramic is therefore expected to wear or eventually crack on the inner surface, next to the mercury column.

4. CONVENTIONAL CERAMIC LINED COPPER TARGET

In this case very different results were obtained compared to the last case. For copper the energy absorbtion was reduced to 250 J in accord with the current thinking regarding the energy absorbtion in the AA copper targets. Figure 10 shows the density variations through the copper and ceramic when the radial dimensions were made equal to the previously discussed case, i.e. copper radius = 1.5 mm, outer ceramic radius = 5.1 mm. The inner zone density progressively decreased with time over the whole of the period covered by the programme ($t < 6078$ ns). Furthermore, distortion of the grid began to appear at 4000 ns until, at the longest times gross variations in the pattern were clearly evident, reminiscent of pinch effects. These are clearly seen in Plot 2, and were most apparent in the low axial zone region where programme input had assumed a rigid container wall of stainless steel. Such distortions were not observed in the mercury target runs, as shown for example in Plot 1 for an unlined mercury target. This is believed to be due to the much higher wave velocities which occur in copper compared with mercury.

The stresses and strains of the vessel are shown in Fig. 11a) and display clearly an oscillating behavior which mirrors the radial displacement at mesh point 16, shown in Fig. 11b) where negative γ positive values are seen. The stresses change from tension to compression and back again within a time of 5000 ns with maximum values occurring at 1500, 3100 and 4300 ns, corresponding to the peaks and troughs of the displacement curve. The angular strain was much higher in the copper target container, peaking at 2×10^{-2}, compared with a value of less than 10^{-3} for mercury. Similarly the angular and axial stresses were an order of magnitude higher for copper than mercury which is consistent with higher pressures and shock wave velocities.

The radial strain, both in the ceramic and the copper, is shown in Fig. 12, and these curves may be directly compared to those for mercury, shown in Fig. 9. The copper values are very much higher, especially at the copper ceramic interface, and should undoubtedly lead to rapid deterioration of the inner surface of the ceramic. This prediction has been verified by recent microscopic examination of passive targets, undertaken by the metallurgical group in CERN.

5. PRE-STRESSED COPPER TARGET

The input data for this target required three major changes from the conventional copper target, namely:

a) changes to the radial zone dimensions of the ceramic to be in accord with the new dimensions.

b) introduction of individual pressures in the copper and ceramic due to the pre-stressed nature of this target. Values of these pressures were calculated from information supplied by F. Gamba.

c) move from a stainless steel vessel of relatively small thickness to a titanium vessel of wall thickness 4.5 cm and with appropriate changes to the physical property input data.

The density of the radial zones showed very similar behavior to that of the conventional copper target, there being a progressive decrease in the inner zone density with time, as shown in Fig. 10. The angular stresses and strains also showed similar behavior in that they were oscillatory in nature, beginning as tensile and gradually becoming compressive, as shown in Fig. 13. Their magnitude was also of the same order as before, however they were shifted to longer times because of the greater thickness of ceramic which had to be crossed by the shock wave. Typically, the first maxima was shifted to t = 3900 ns whilst before, in the conventional target, it occurred at t = 1500 ns. These values are reasonably in accord with expectations since the ceramic thickness was now 0.84 cm compared to 0.35 cm in the conventional target.

The radial strains in the ceramic were found to be very high as shown in Fig. 14, and were far greater than the levels usually quoted in the literature. It is therefore strongly possible that the ceramic will shatter under the combined effects of the beam on the copper and its own pre-stressing.

The final sets of computations were made with the mercury target and the conventional copper target in which the target material was divided into four distinct zones as shown below, into which different amounts of energy were deposited. In each case the total energies absorbed were as before, but were distributed as also shown, in brackets

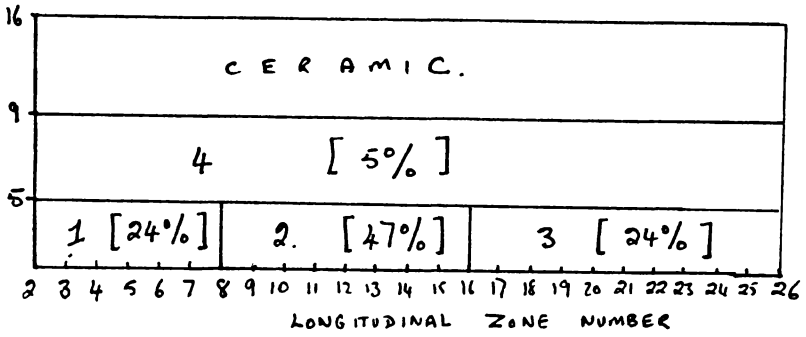

The result of this preferential energy deposition was to produce results for all outputs which, in both cases, showed axial as well as radial dependence. Of greatest interest is the distortion of the mesh which is shown in Plot 3 for mercury and Plot 4 for copper. It is very clearly seen, in the latter case, that the distortion first occurs in the inner radial zones, between axial zones 9 and 16 and that it then spreads out axially, towards the ends of the target cylinder.

In the case of vessel stress and strains, which up to now had been axially independent, there was a rapid variation from compressive at low axial numbers to tensile in the middle, reverting back to compressive at the other end and this is shown in the two cases, for angular vessel stress, in Fig. 15. It is as if the vessel were being distorted as follows:

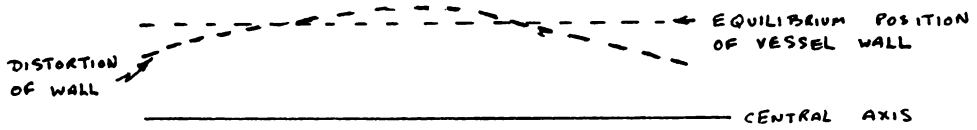

6. PRE-STRESSED TARGET. REAL DEPOSITION OF ENERGY, IN MERCURY AND SOLID INDIUM AND COPPER

Final calculations were made on liquid mercury and solid copper and indium in which the energy deposition was spread non-uniformly over the target zones, as indicated in the previous section. The total energy deposited in the three cases were a) mercury 2 kJ, b) indium 1 kJ and c) copper 500 J, which are in fair agreement with the values quoted by Aarnio[3], assuming a target length of 100 mm.

The variation of the normalized target density in the inner zones, is shown in Fig. 16 and shows interesting differences between the behavior of "solid" and liquid materials. The density of mercury shows the same oscillatory behavior previously shown in Figs 3a), 3b) and 5, whereas both indium and copper show a gradual decrease in central zone density, approaching asymptotic values of 25% and 40% respectively, after about 4000 ns.

The stresses and strains in the titanium vessel are shown in Fig. 17 and are much higher for the solid materials than for mercury and also peak at earlier times after energy deposition. The differences in these curves are similar in nature to those shown in Figs 8 and 11, for the conventional geometry. The three curves shown for mercury were obtained by increasing the ceramic thickness in the programme, at the expense of the titanium, the outer radius of which was kept constant. In the three cases the ceramic thickness was:

$$\text{Hg 1} \begin{cases} r = 10 \text{ mm}, \\ r_{tit} = 30 \text{ mm}, \end{cases} \quad \text{Hg 2} \begin{cases} r = 11.4 \text{ mm} \\ r_{tit} = 28.6 \text{ mm} \end{cases} \quad \text{and Hg 3} \begin{cases} r = 14 \text{ mm} \\ r_{tit} = 26 \text{ mm} \end{cases}$$

The effect of this change was merely to shift the strain maximum to longer times, without appreciably altering the maximum value. This presumably is because the increasing effect of decreasing the titanium thickness is compensated for by the extra shielding effect of the greater thickness of ceramic.

The time evolution of the radial strains in the ceramic are shown for mercury on Fig. 18, and indium in Fig. 19. Both reveal a rise to a maximum value and then a gradual decrease. However, in the solid indium the values are extremely high, especially at the inner surface, and indicate that the ceramic is being subjected to intolerable short term conditions due to the shock wave. The effect is an order of magnitude lower in mercury in spite of the higher energy inputed to the target. Furthermore, it was found that in the solid materials there was a significant axial strain which was not apparent in the liquid case.

7. PRELIMINARY CONCLUSIONS

It is believed that

a) the use of a REXCO shock wave program has been successfully applied to the case of solid and liquid antiproton targets. Whilst "black boxes" still exist, much of the predictions of the program can be physically understood and trusted.

b) predictions of the program, in the case of a simple enclosed mercury column, are as expected and could provide hope that, with a ceramic of gradually increasing bore, self pumping of the mercury could be possible, although no precise calculations have been made to verify this.

c) very large radial strains exist in the components of the conventional copper target, especially at the copper ceramic interfact which agree with the damage observed in metallurgical examination of such targets. Pinch distortion effects have also been observed in the copper at long times after energy injection, which were not apparent with mercury.

d) the stresses and strains of the vessel in the conventional Cu target and the pre-stressed Cu target are oscillatory in nature. High radial strains also exist at the copper-ceramic interface of the pre-stressed target which could produce the same damage as observed in the conventional target. Hydrostatic loading does not appear to prevent dynamic separation of copper and ceramic. Non-axial uniformity of the container response, combined with the magnetic field induced pinch may lead to axial flow of the copper.

e) both solid targets display a non return to normal central zone density over the time of computation and, if this effect is cumulative, one might conclude that the $p/\bar{p}$ efficiency would decrease with time, due to this, combined with metallurgical deterioration or change in structure of the target.

f) the effect of inputing all of the beam energy in at $t = 0$ is probably to enhance the peak effects on ceramic radial strains and vessel stresses and strains. It is recognized that the program should be modified to allow, for example, the deposition of energy in as five equal bursts having an individual separation of 100 ns.

g) sufficient evidence exists to suggest that a liquid metal target has more chance of long term survival than a solid one, especially if the enclosure problem is overcome by containing the liquid metal in a closed circuit or pre-pressurized tantalum or titanium system.

8. REFERENCE

1. Y.W. Chang, J. Guildys and S.H. Fistedis, Two-dimensional Hydrodynamic Analysis for Primary Containment, Argone National Laboratory,

2. Thiel, Kusabov and Mitchell, Compendium of Shock wave Data, Lawrence Radiation Laboratory, October 1957.

3. P.A. Aarnio, Heating of the Antiproton Production Target, TIS-RP/IR/84-52.

FIG 1 a)

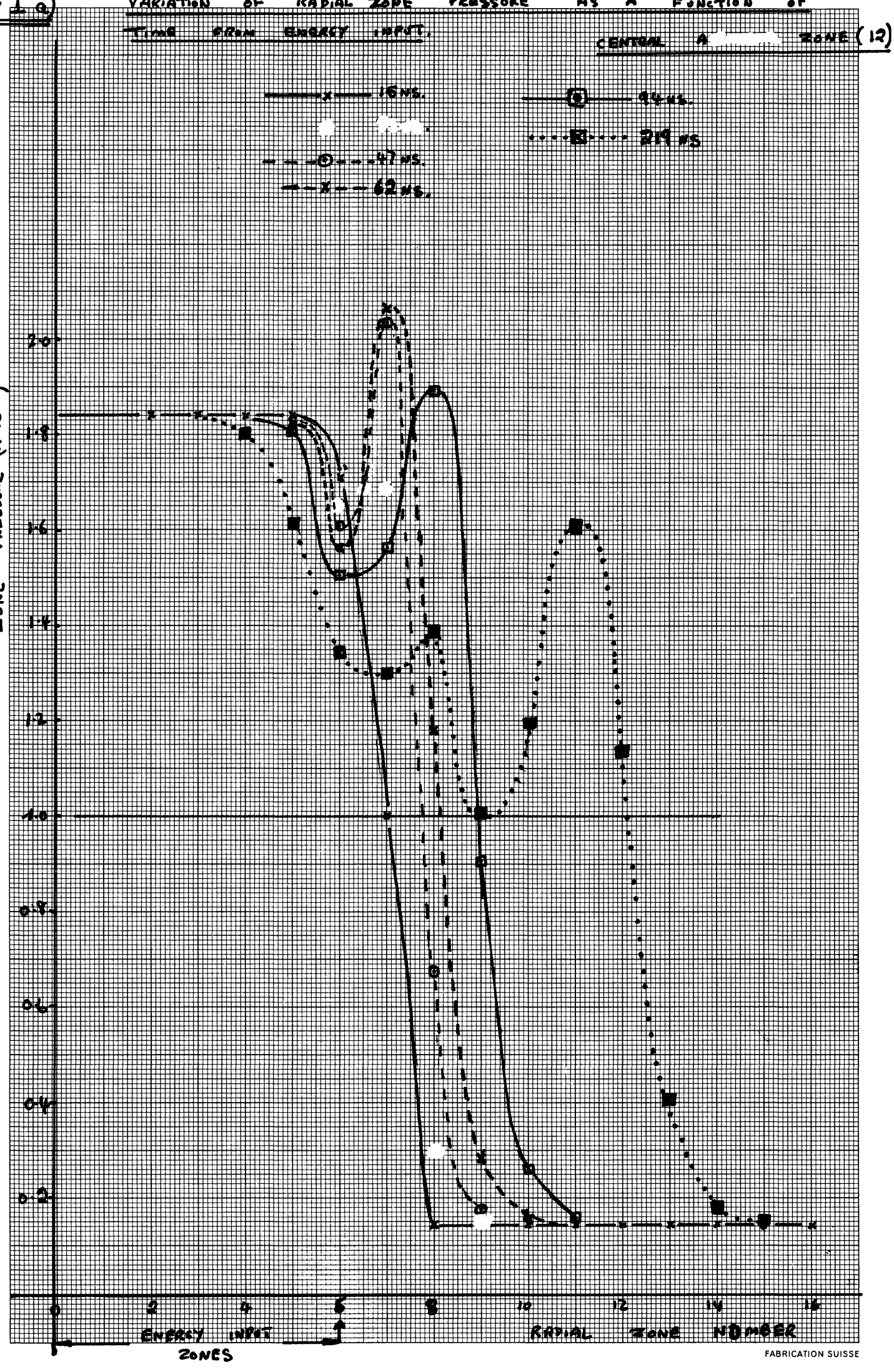

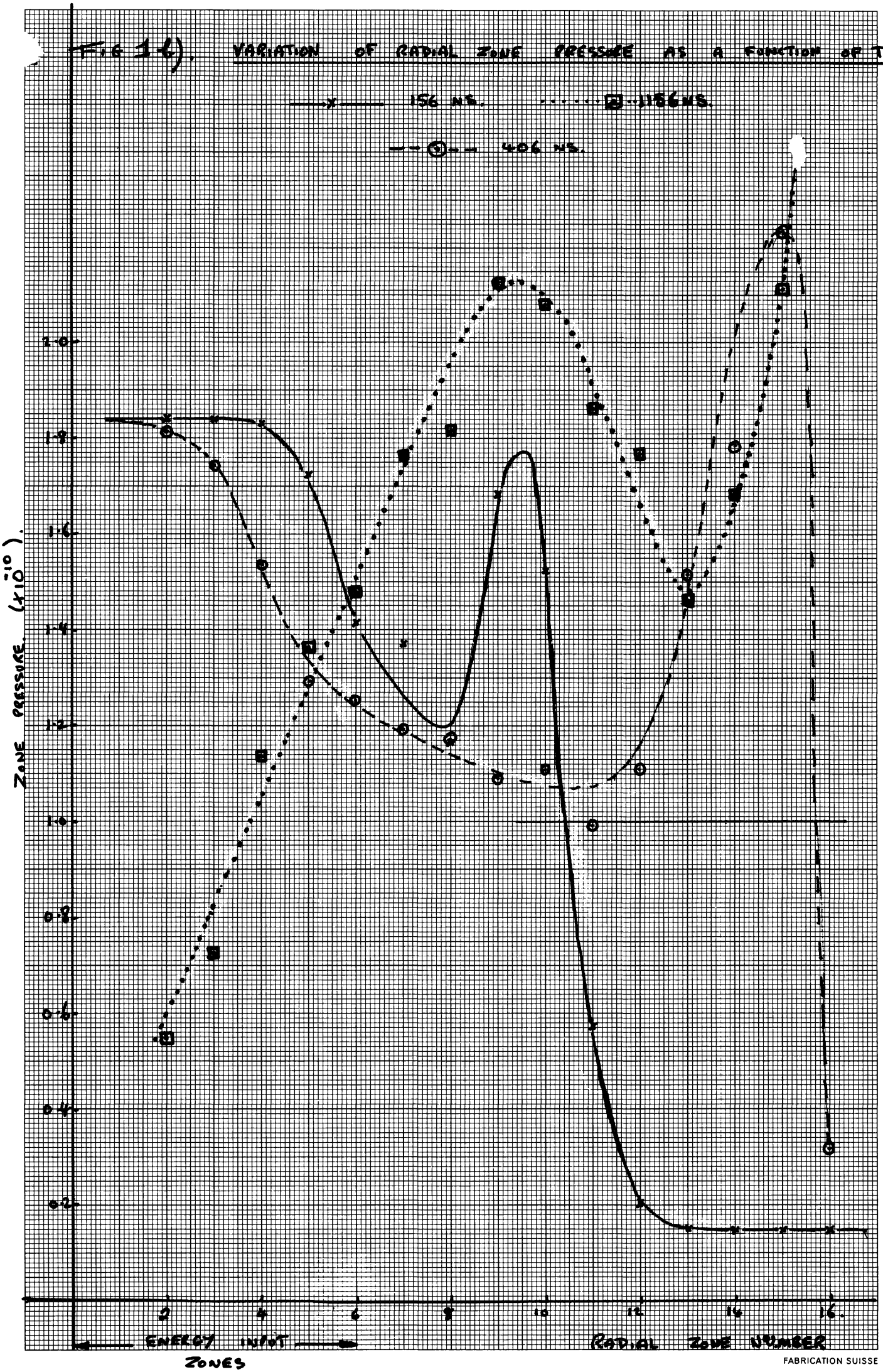
FIG 14). VARIATION OF RADIAL ZONE PRESSURE AS A FUNCTION OF TIME
156 MS.
1186 MS.
406 MS.
ZONE PRESSURE (x10⁻¹⁰).
2·0
1·8
1·6
1·4
1·2
1·0
0·8
0·6
0·4
0·2
2
4
6
8
10
12
14
16
ENERGY INPUT ZONES
RADIAL ZONE NUMBER
FABRICATION SUISSE

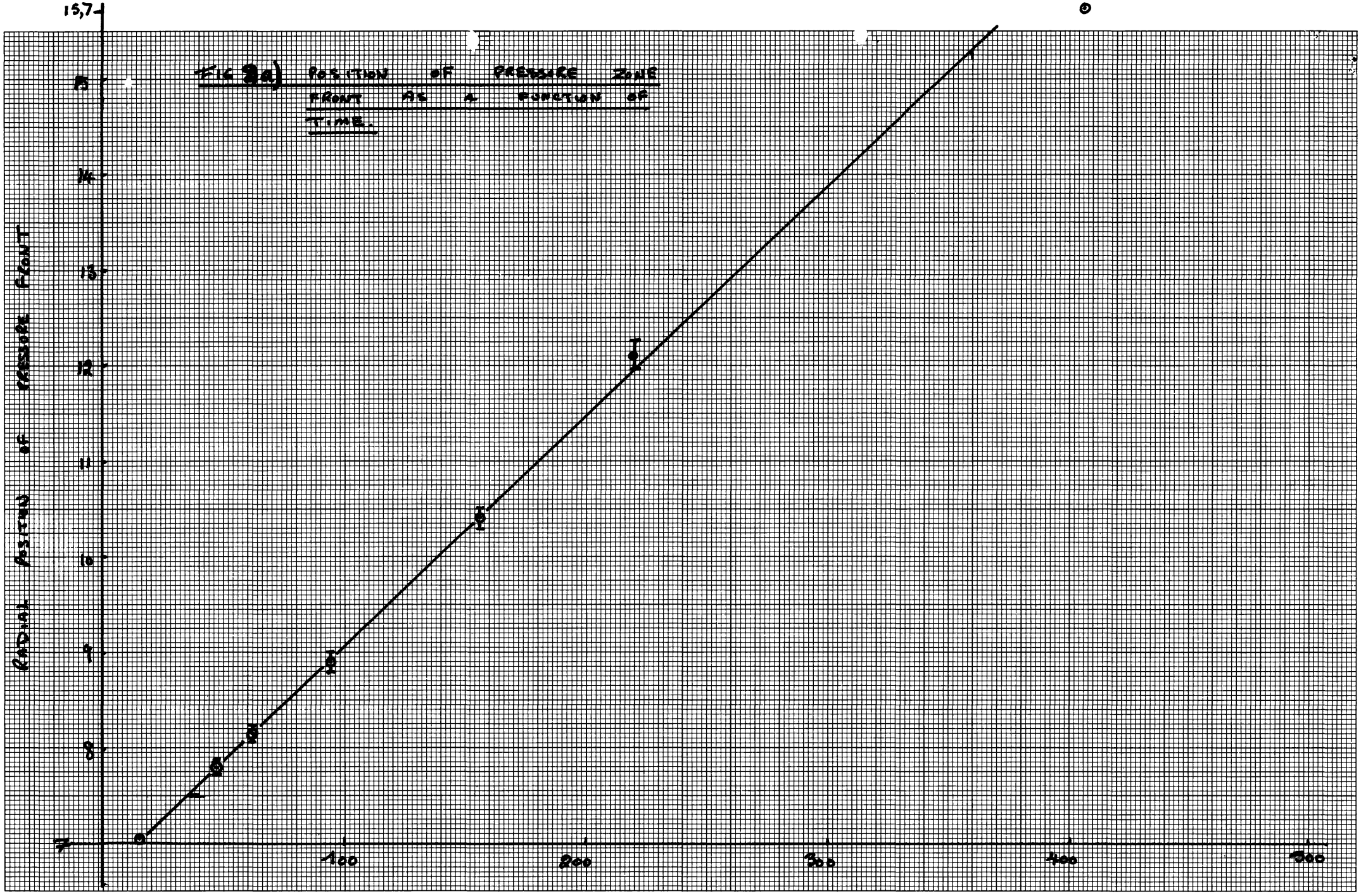

Fig 3a) Position of pressure zone front as a function of time.

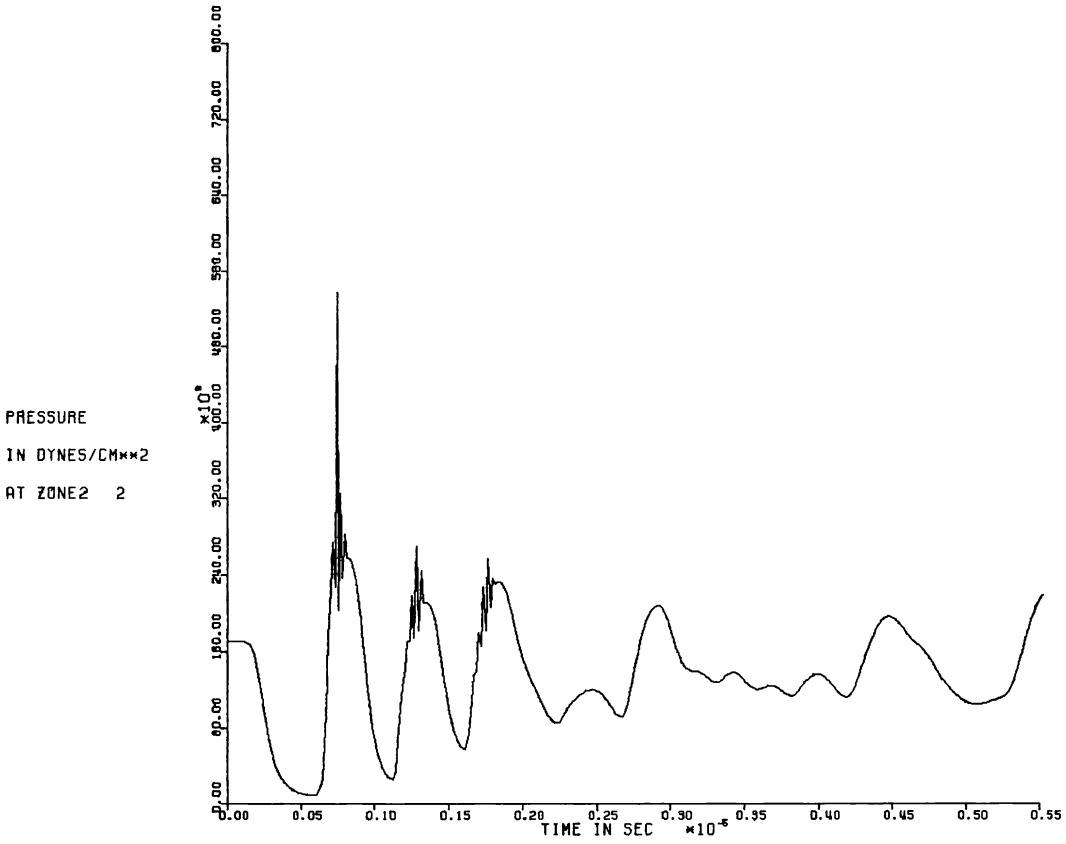

FIG 21) PRESSURE VARIATION IN CENTRAL RADIAL ZONE AS A FUNCTION OF TIME.

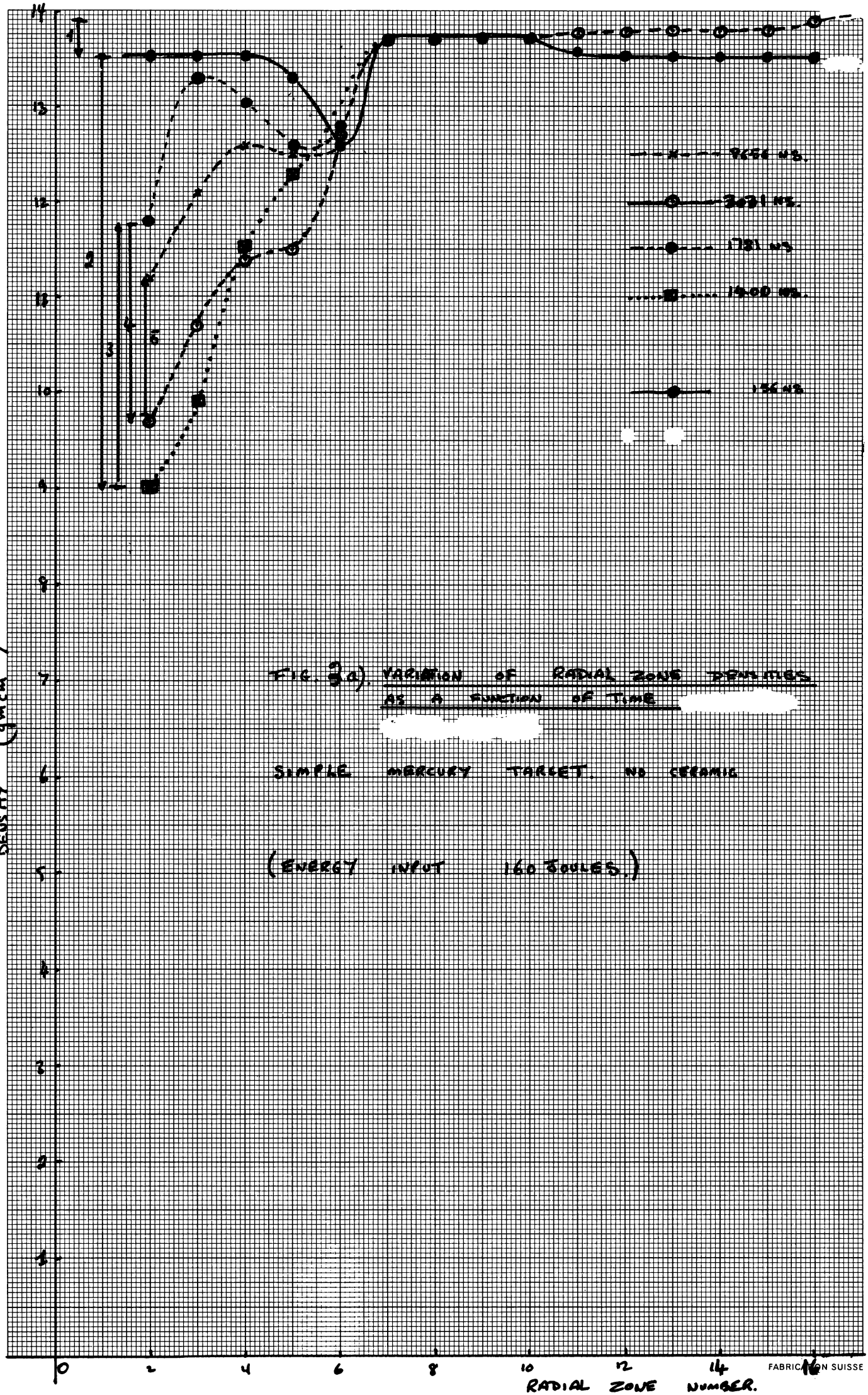

FIG. 9 a). VARIATION OF RADIAL ZONE DENSITIES AS A FUNCTION OF TIME

SIMPLE MERCURY TARGET. NO CERAMIC

(ENERGY INPUT 160 JOULES.)

FIG 3B) VARIATION OF RADIAL ZONE DENSITIES AS A FUNCTION OF TIME.

(ENERGY INPUT 1600 J). MERCURY TARGET. NO CERAMIC.

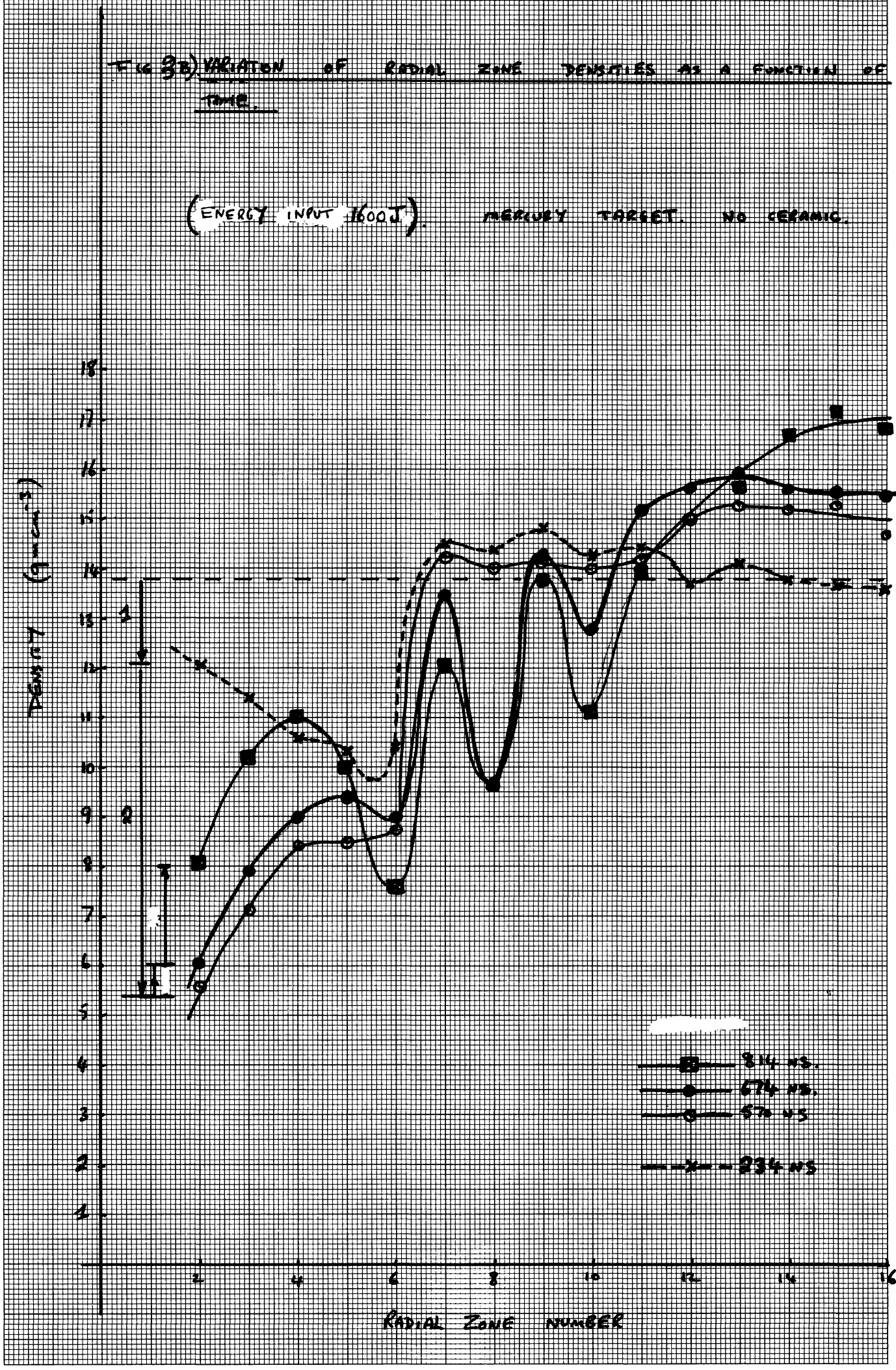

FIG 4a) SIMPLE MERCURY COLUMN. LONG TERM EFFECTS ON STRESSES & STRAINS IN VESSEL.

$E_0 = 1600\ J$

ANGULAR STRAIN.

AXIAL STRESS.

ANGULAR STRAIN $\left(\frac{\Delta l}{l}\right)$

AXIAL STRESS (dyne cm^{-2})

TIME FROM DEPOSITION OF ENERGY (NS)

FIG 4b) RADIAL DISPLACEMENT OF MESH POINT 16 AS FUNCTION OF TIME.

RADIAL DISPLACEMENT AT MESH POINT 16.

TIME IN SEC $\times 10^{-6}$

FIG 5. VARIATION OF RADIAL ZONE DENSITIES AS A FUNCTION OF TIME, WITH A CERAMIC INSERT

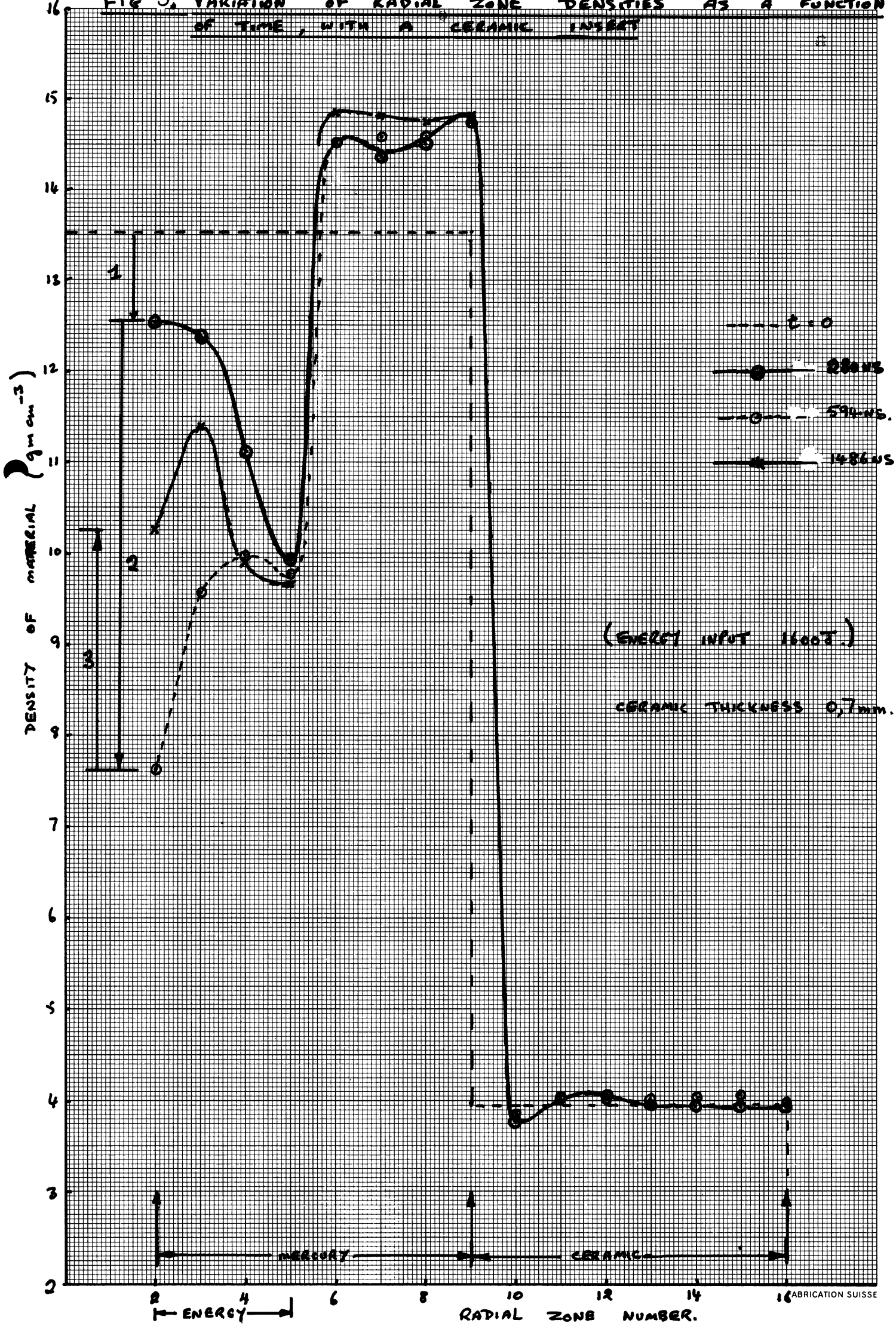

A. West & Partners Ltd.
36, Broadway, Westminster, S.W.1

Data Sheet No. 14. Logarithmic (3 Cycle) × 120 Divisions

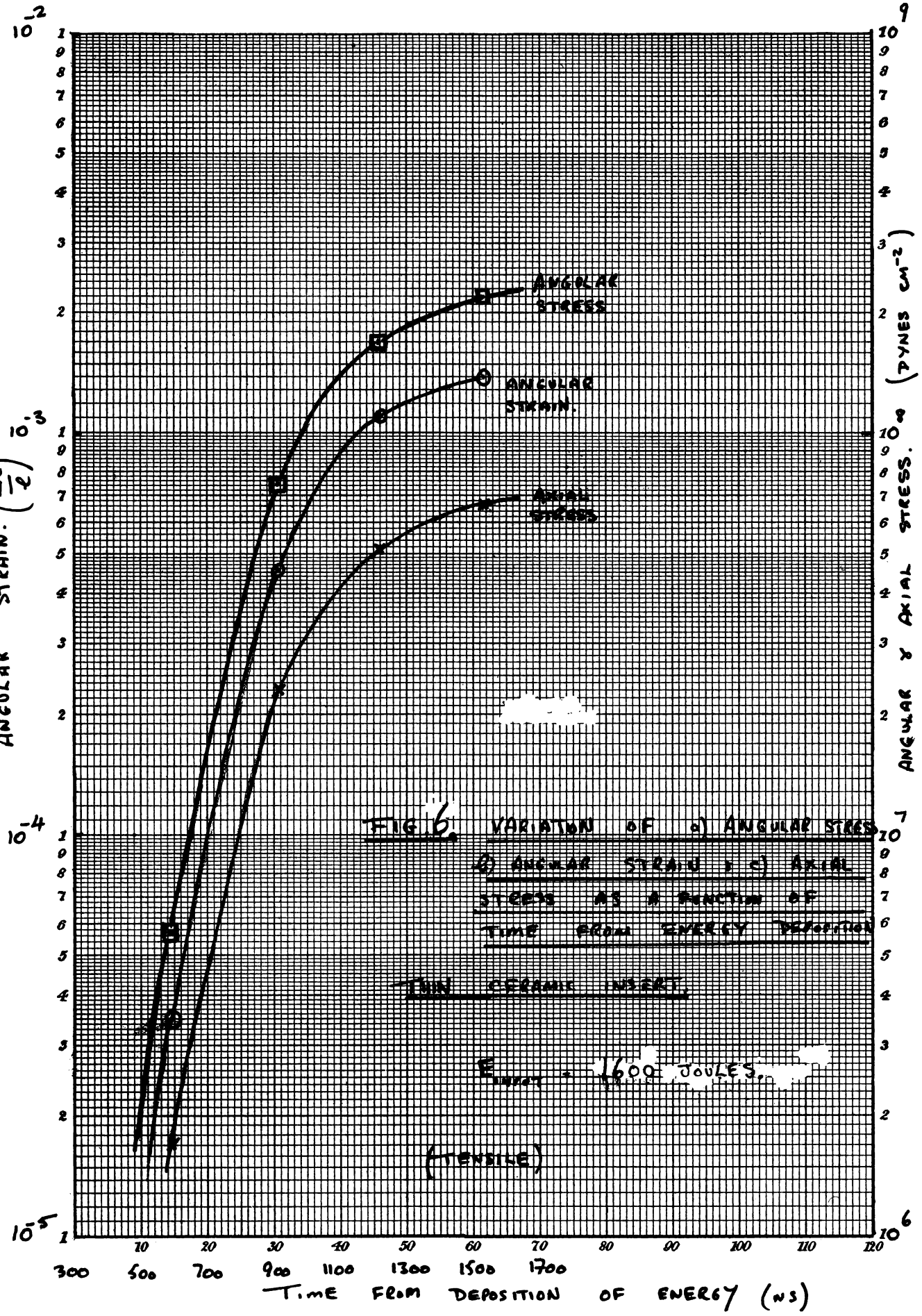

FIG. 6. VARIATION OF a) ANGULAR STRESS, b) ANGULAR STRAIN & c) AXIAL STRESS AS A FUNCTION OF TIME FROM ENERGY DEPOSITION IN THIN CERAMIC INSERT.

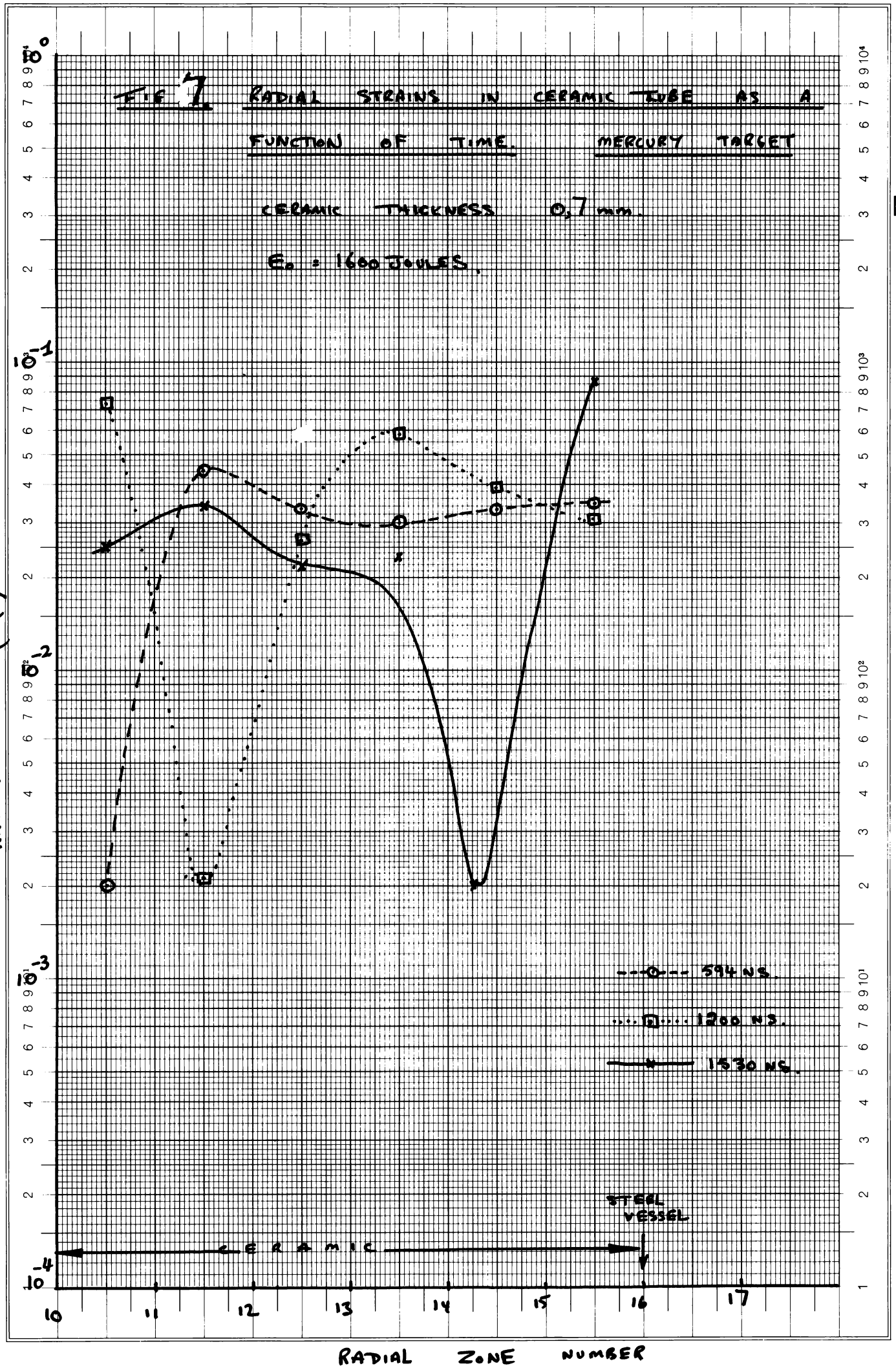

FIG 8a) ANGULAR & AXIAL STRESSES & STRAINS OF VESSEL AS A FUNCTION OF TIME FROM ENERGY INPUT

E_0 = 1600 JOULES. MERCURY TARGET

THICK CERAMIC.

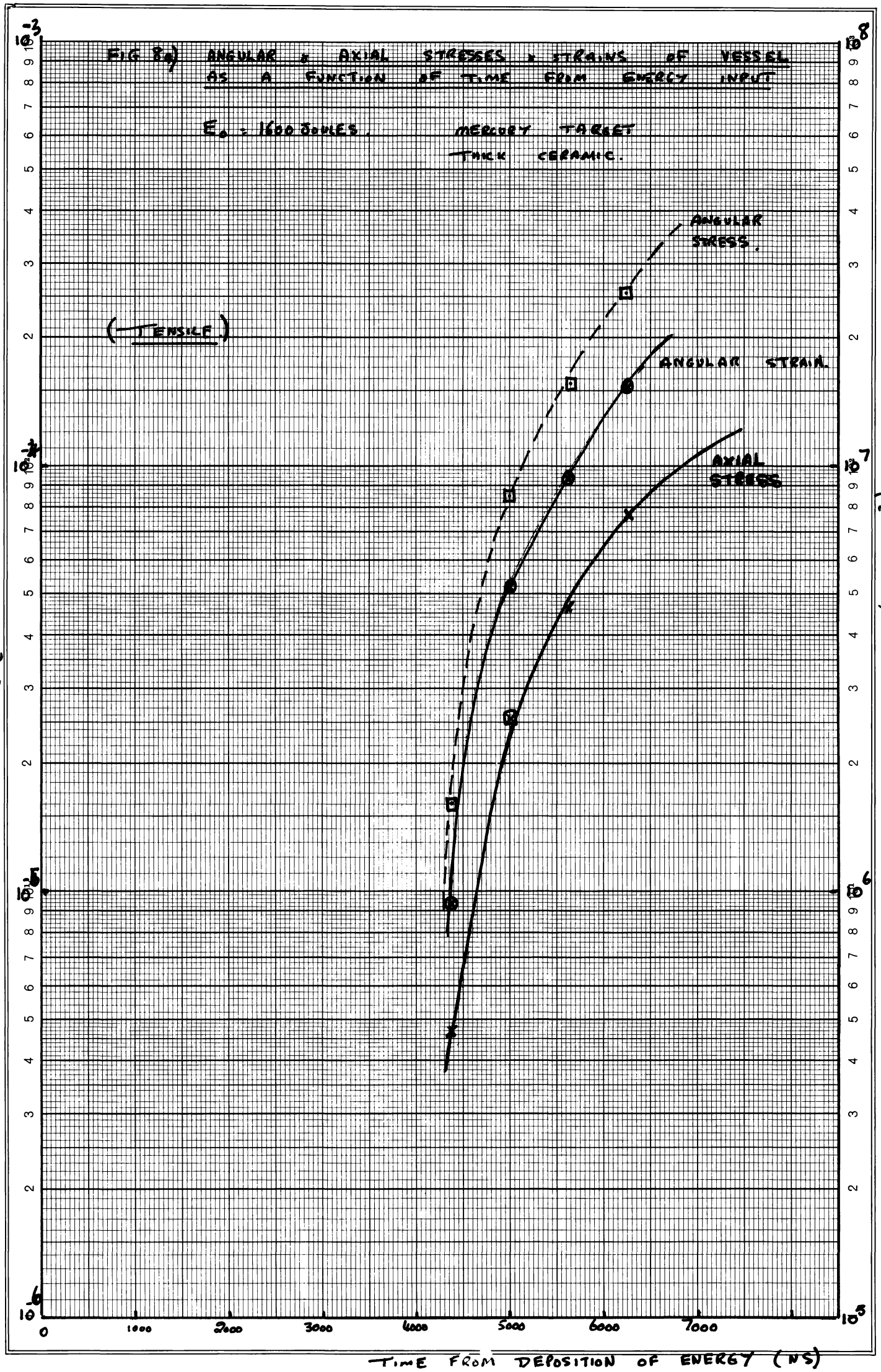

Logar. Teilung / Division } 1 - 1000 Einheit / Unité } 90 mm

MERCURY TARGET $E_0 = 1600\ J$.

THICK CERAMIC.

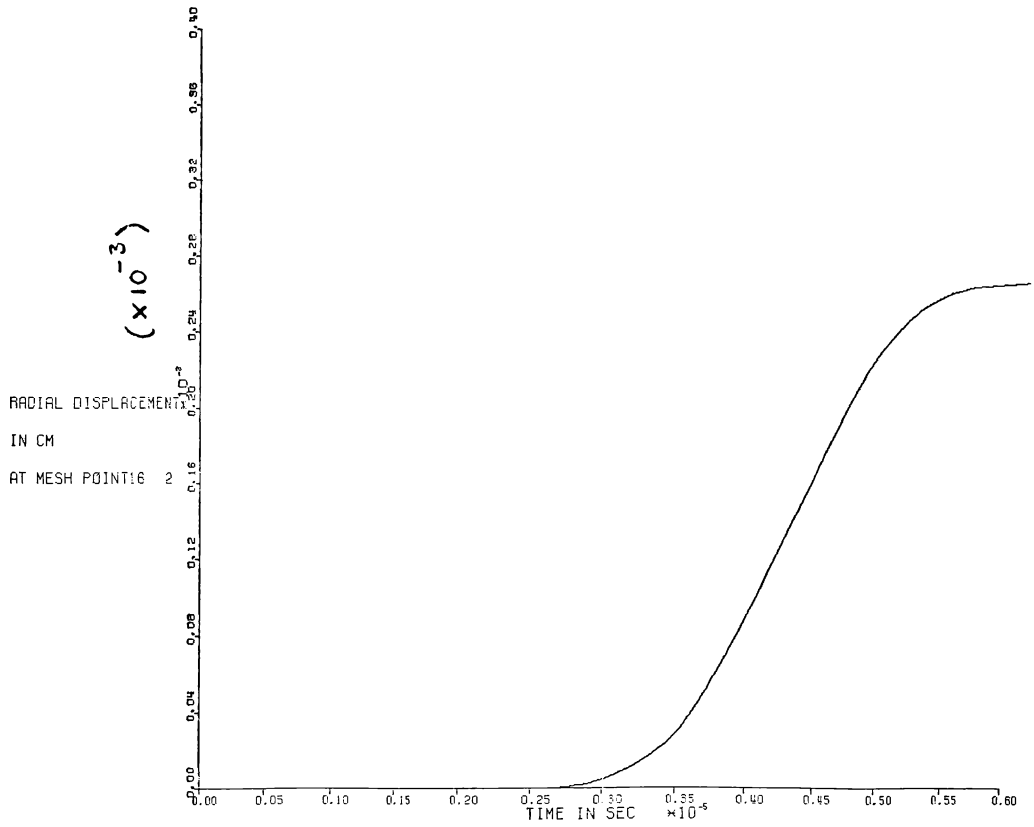

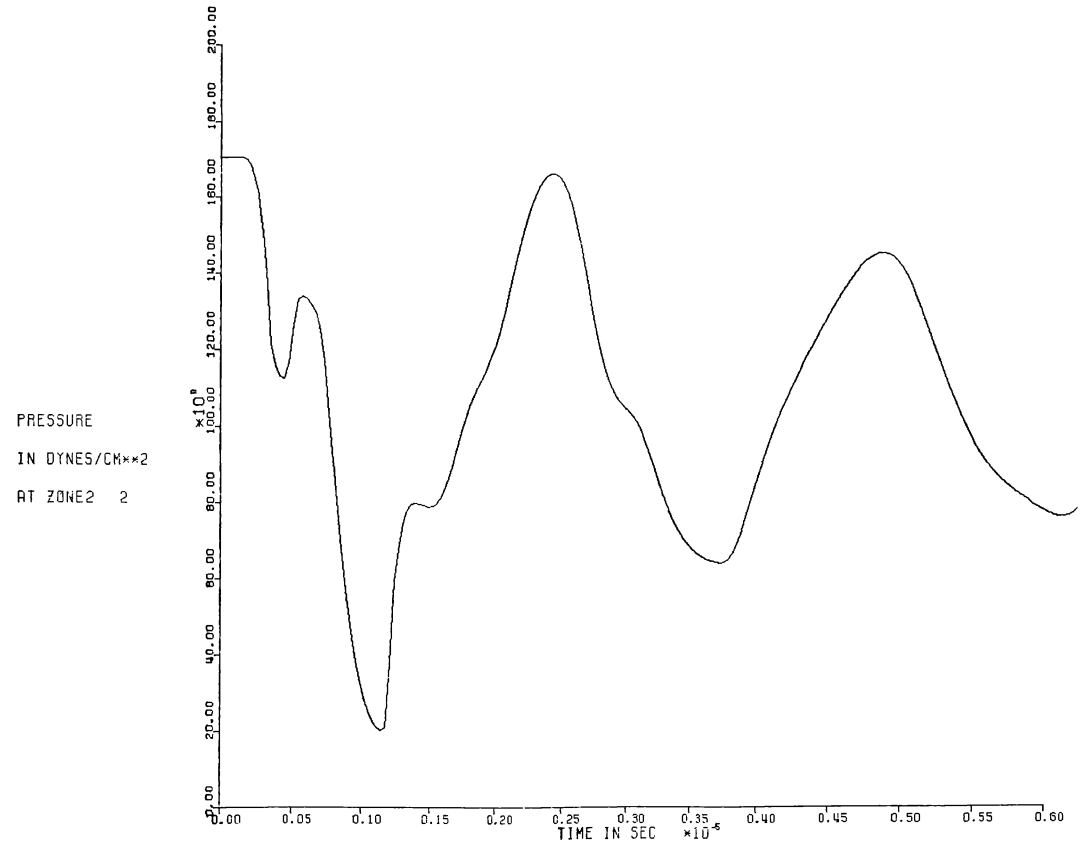

FIG 8-b) RADIAL DISPLACEMENT (ZONE 16) AND PRESSURE (ZONE 2) AS A FUNCTION OF TIME.

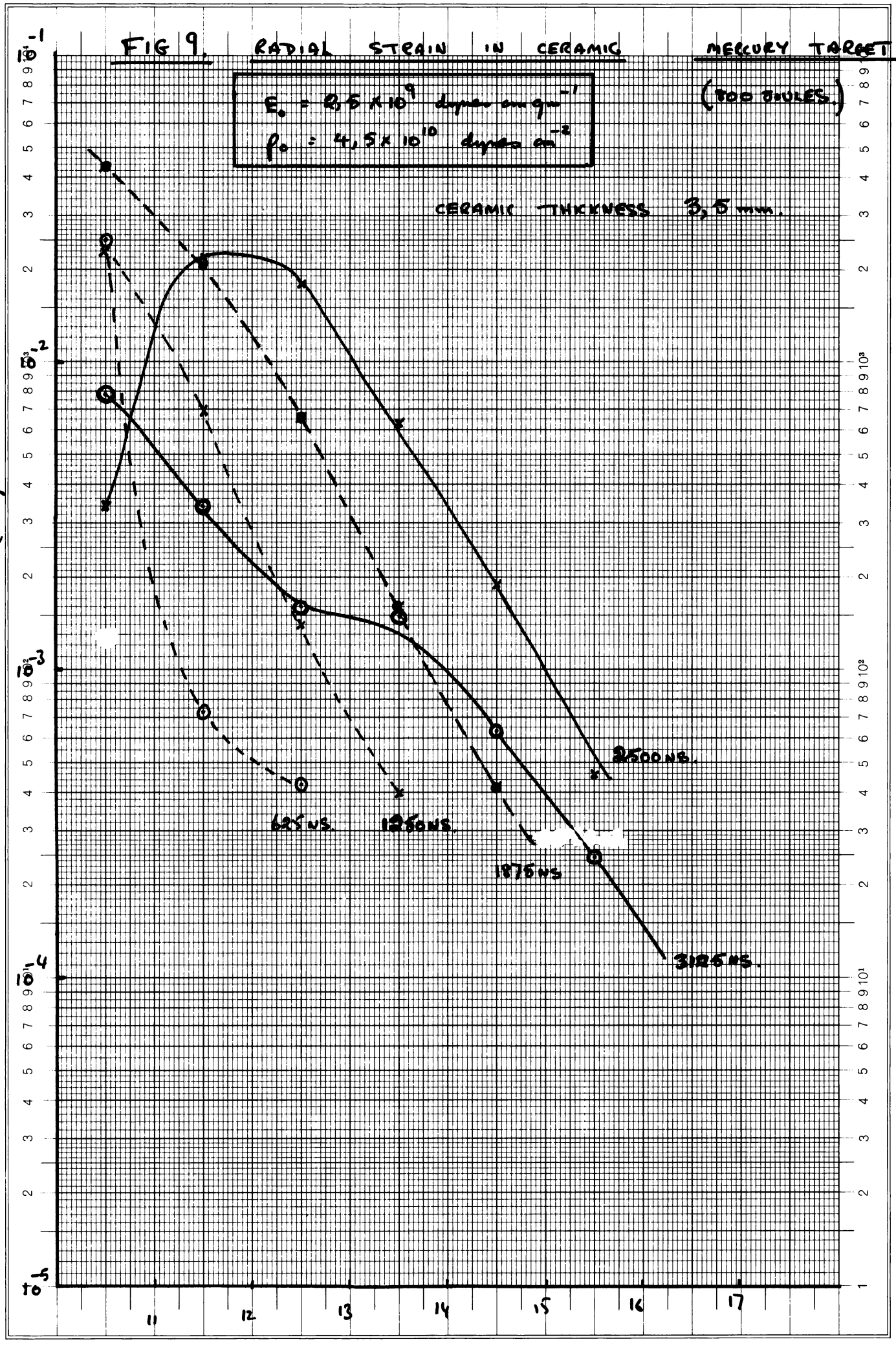

Ed. Aerni-Leuch, Bern Nr. 526

Logar. Teilung { 1-10000 Einheit { 62,5 mm
Division { Unité

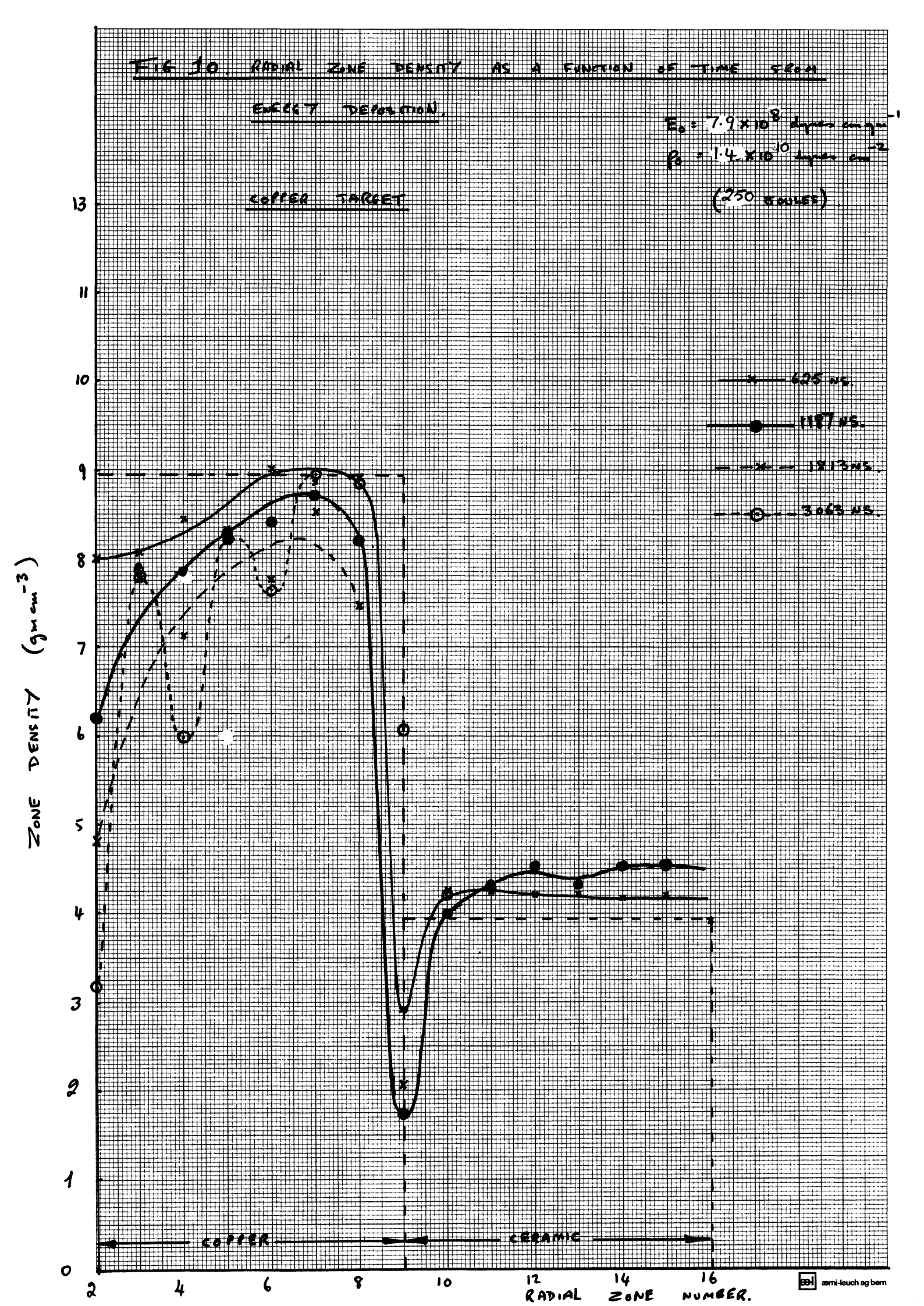
FIG 10 RADIAL ZONE DENSITY AS A FUNCTION OF TIME FROM
EXCEET DEFLECTION.
COPPER TARGET
$E_0 = 7.9 \times 10^8$ dyne cm^{-1}
$P_0 = 1.4 \times 10^{10}$ dyne cm^{-2}
(250 VOLTS)
625 NS.
1187 NS.
1813 NS.
3063 NS.
ZONE DENSITY (gm cm^{-3})
RADIAL ZONE NUMBER.
COPPER
CERAMIC
0
1
2
3
4
5
6
7
8
9
10
11
13
2
4
6
8
10
12
14
16

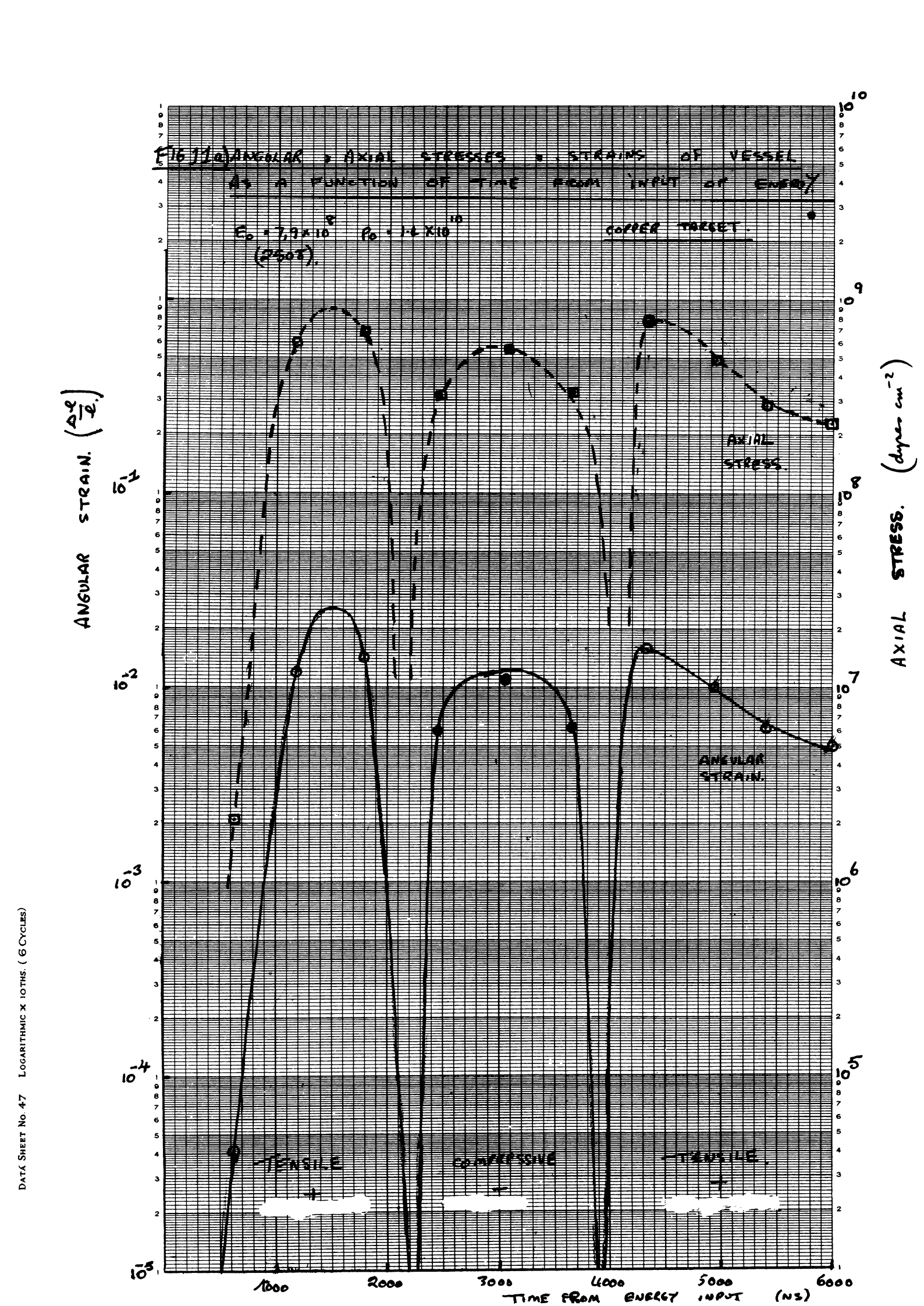

DATA SHEET No. 47 LOGARITHMIC X 10THS. (6 CYCLES)

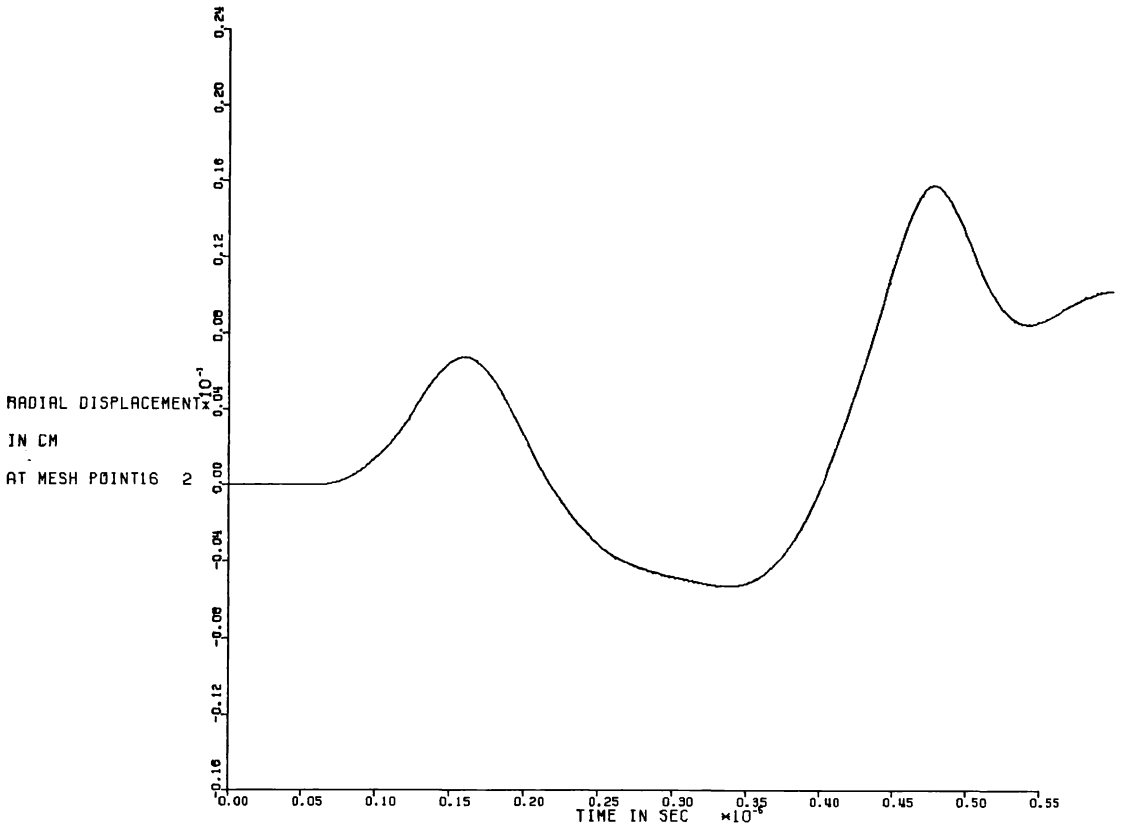

FIG 11-b) RADIAL DISPLACEMENT AT ZONE 16 AS A FUNCTION OF TIME.

COPPER TARGET

E_0 = 250 JOULES

FIG 12 RADIAL STRAIN IN CERAMIC COPPER TARGET

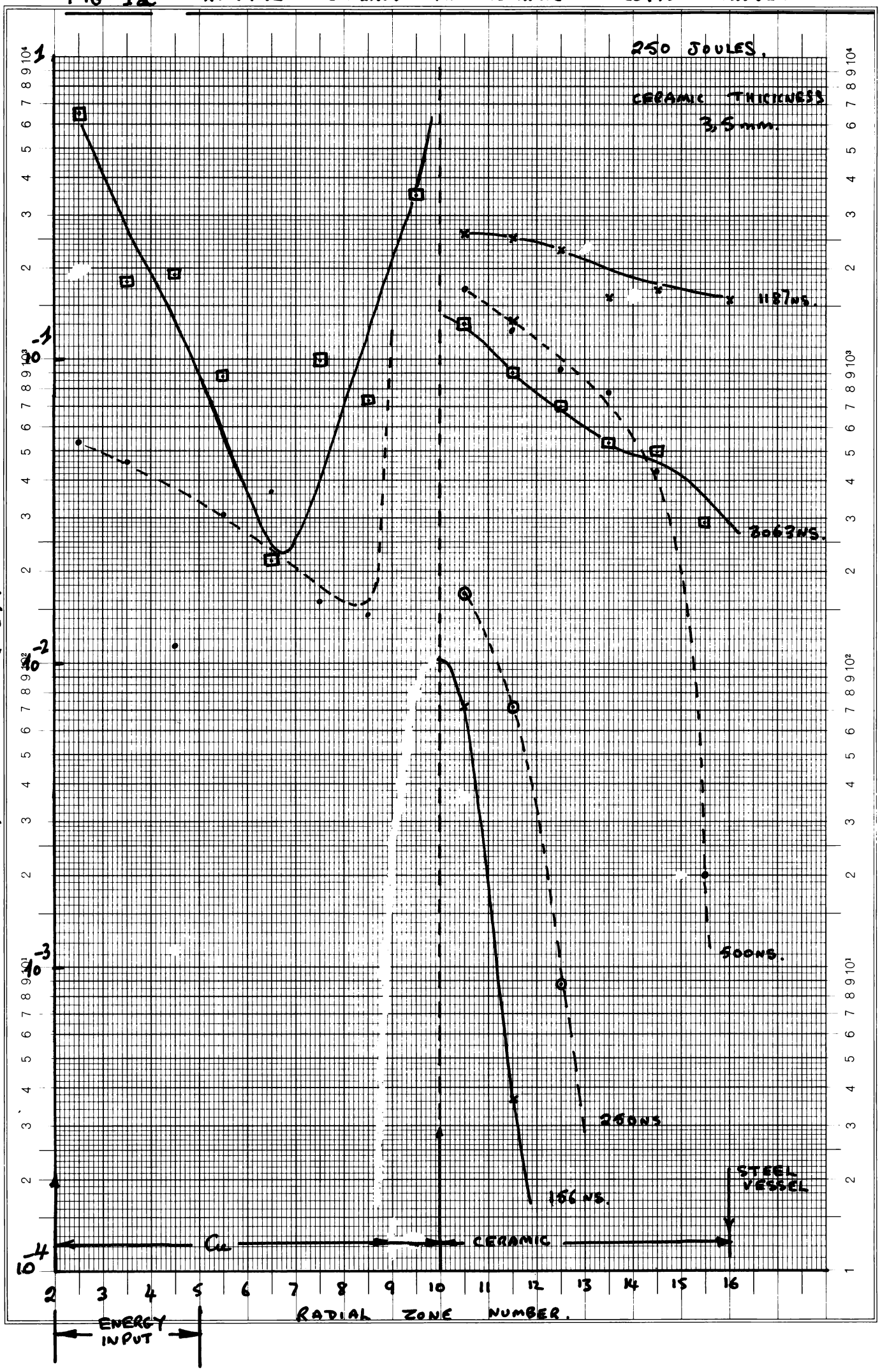

FIG. 19. ANGULAR x AXIAL STRESSES x STRAINS OF VESSEL AS A FUNCTION OF TIME FROM ENERGY INPUT

E_0 = 250 J PRESTRESSED COPPER TARGET.

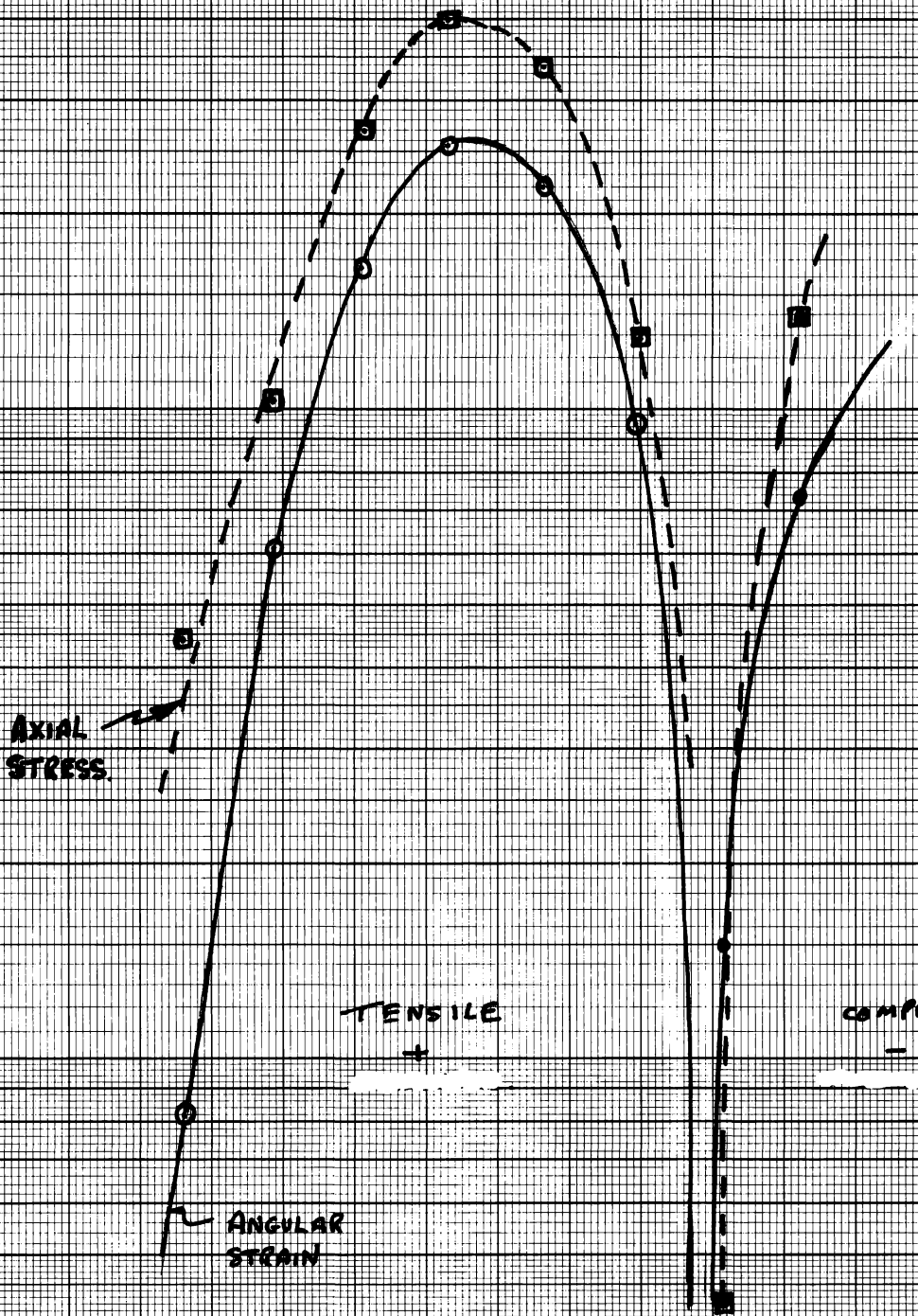

ANGULAR STRAIN $\left(\frac{\Delta\ell}{\ell}\right)$.

STRESS (dyne cm^{-2})

0 1000 2000 3000 4000 5000 6000 7000

TIME FROM ENERGY INPUT (ns)

Logar. Teilung / Division } 1 - 1000 Einheit / Unité } 90 mm

ærni-leuch ag. 3097 liebefeld-bern Nr. 534

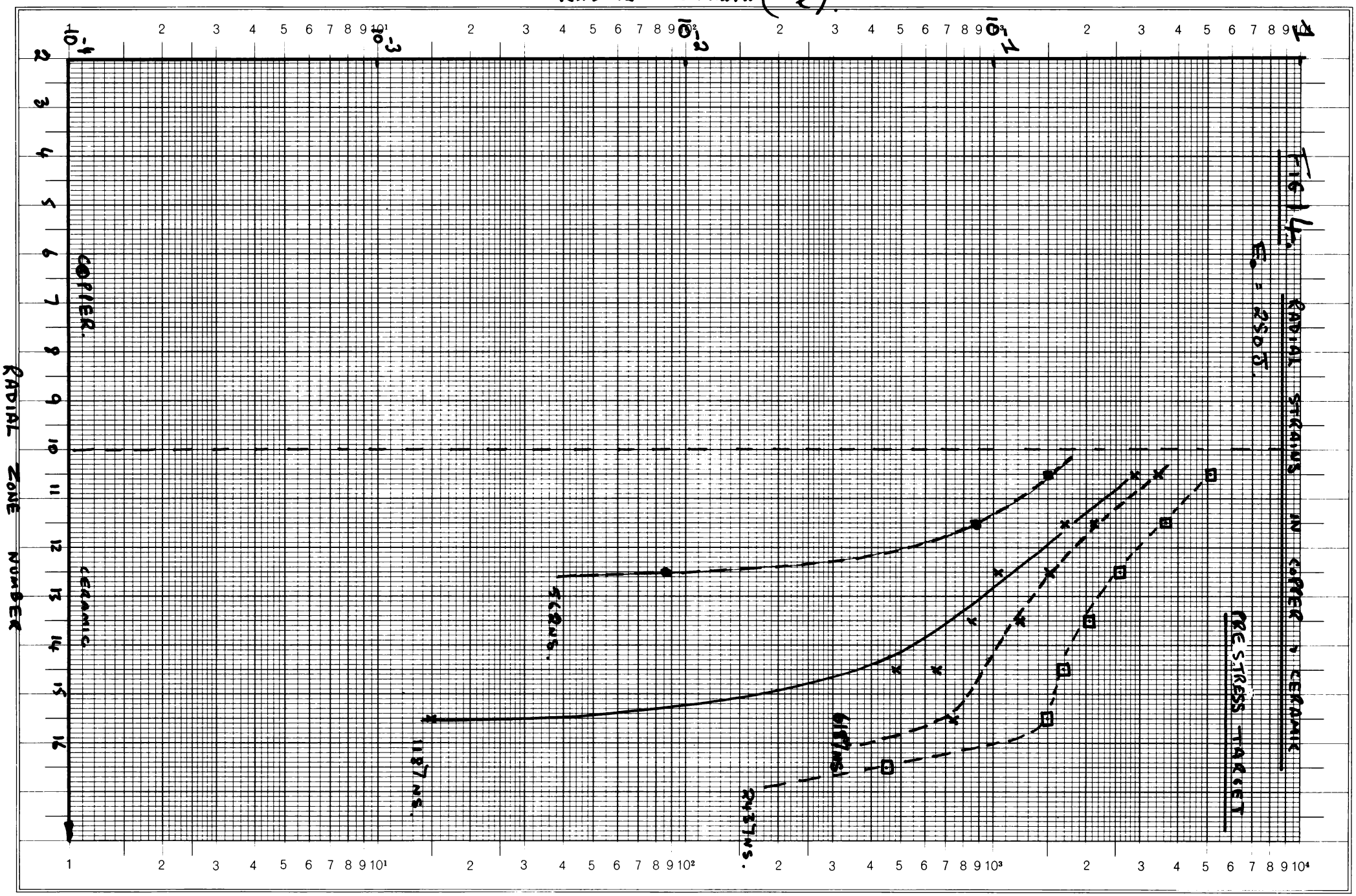

Logar. Teilung / Division } 1-10000 Einheit / Unité } 62,5 mm

arni-leuch ag. 3097 liebefeld-bern Nr. 526

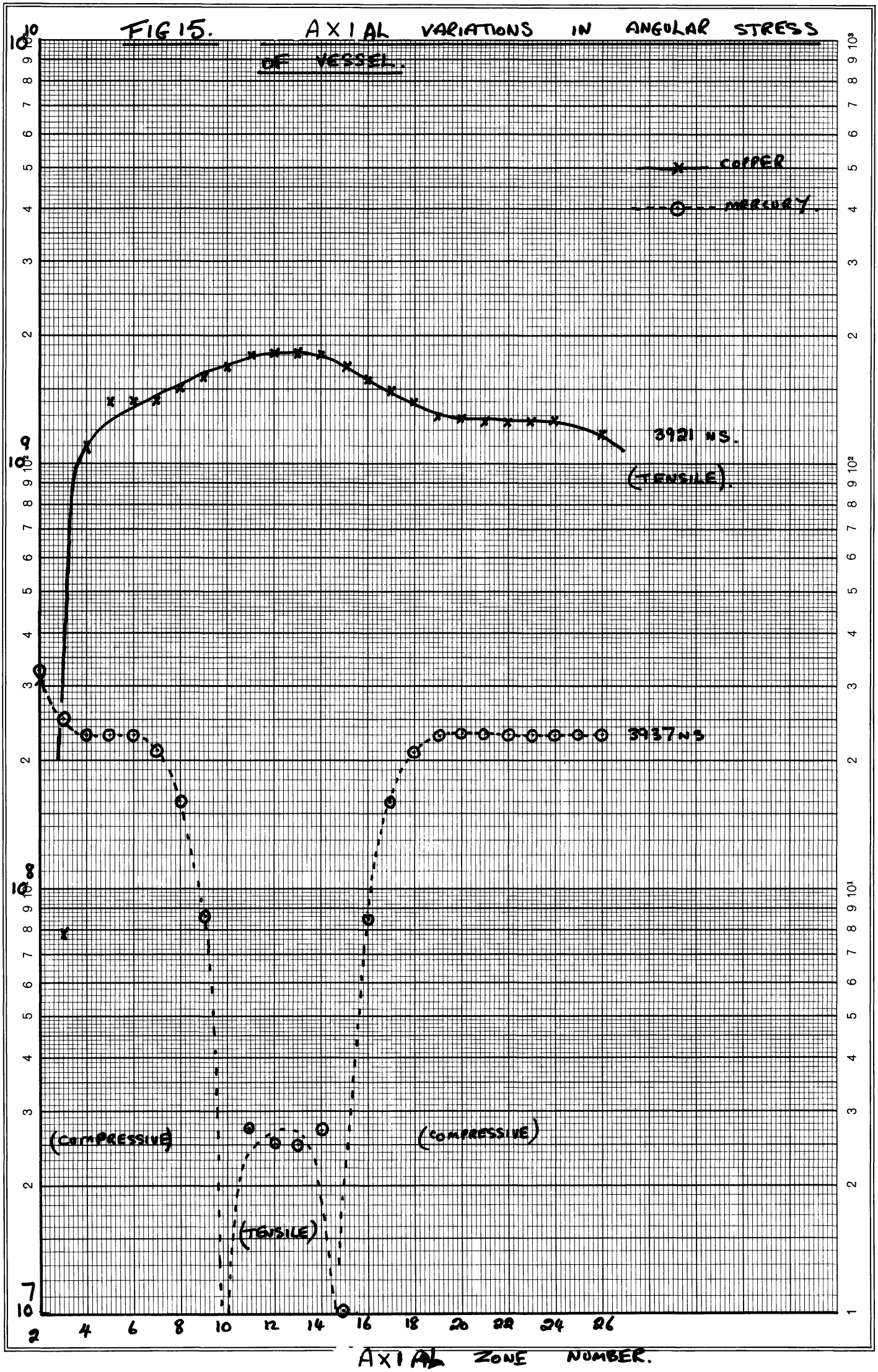

FIG. 16. DEPENDANCE OF AVERAGE NORMALIZED DENSITY OF TWELVE INNER RADIAL ZONES OF TARGET ON TIME FROM ENERGY DEPOSITION.

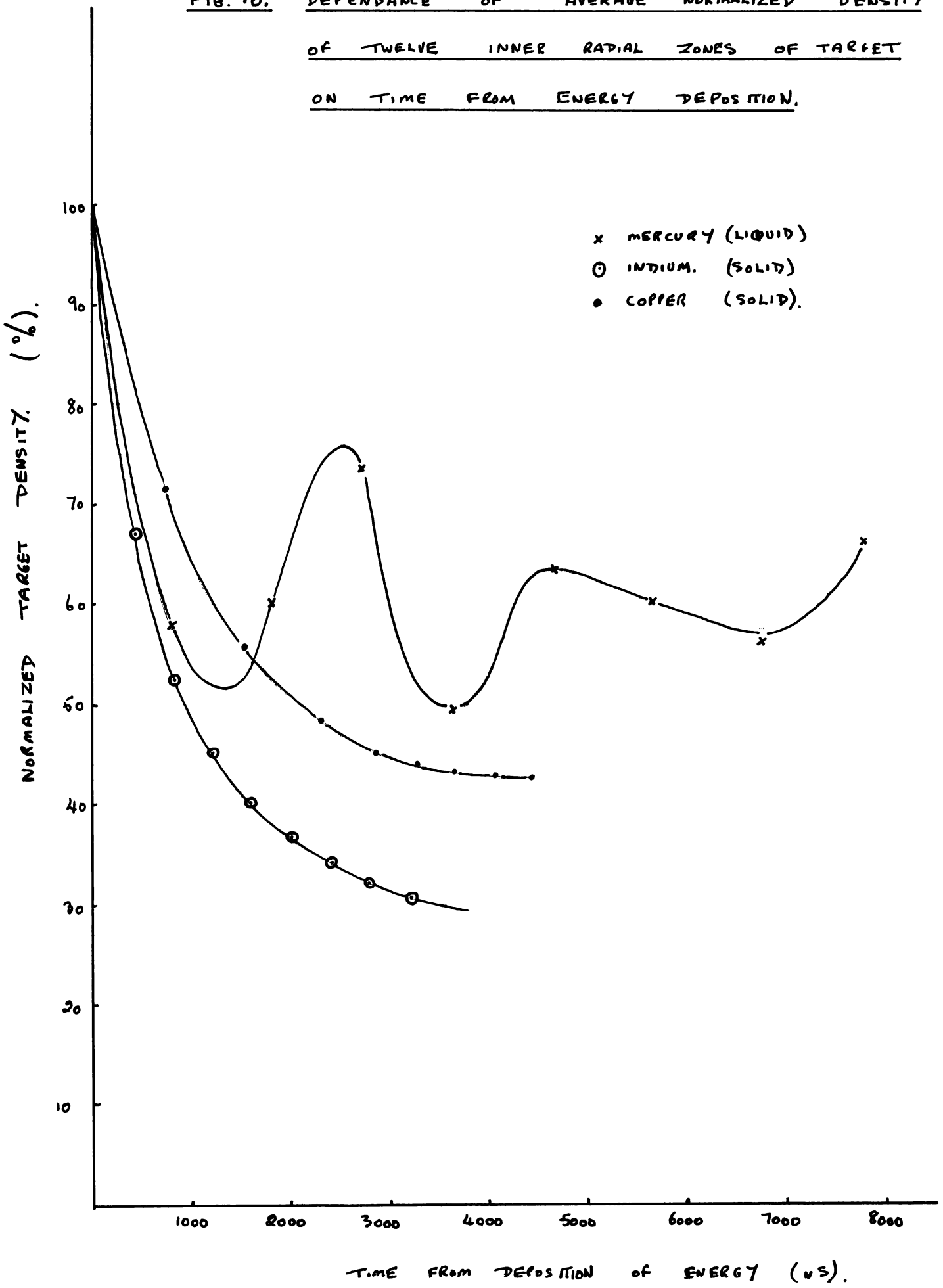

FIG. 17.

ANGULAR STRAINS OF VARIOUS TITANIUM ENCLOSED TARGETS AS A FUNCTION OF TIME FROM DEPOSITION OF ENERGY.

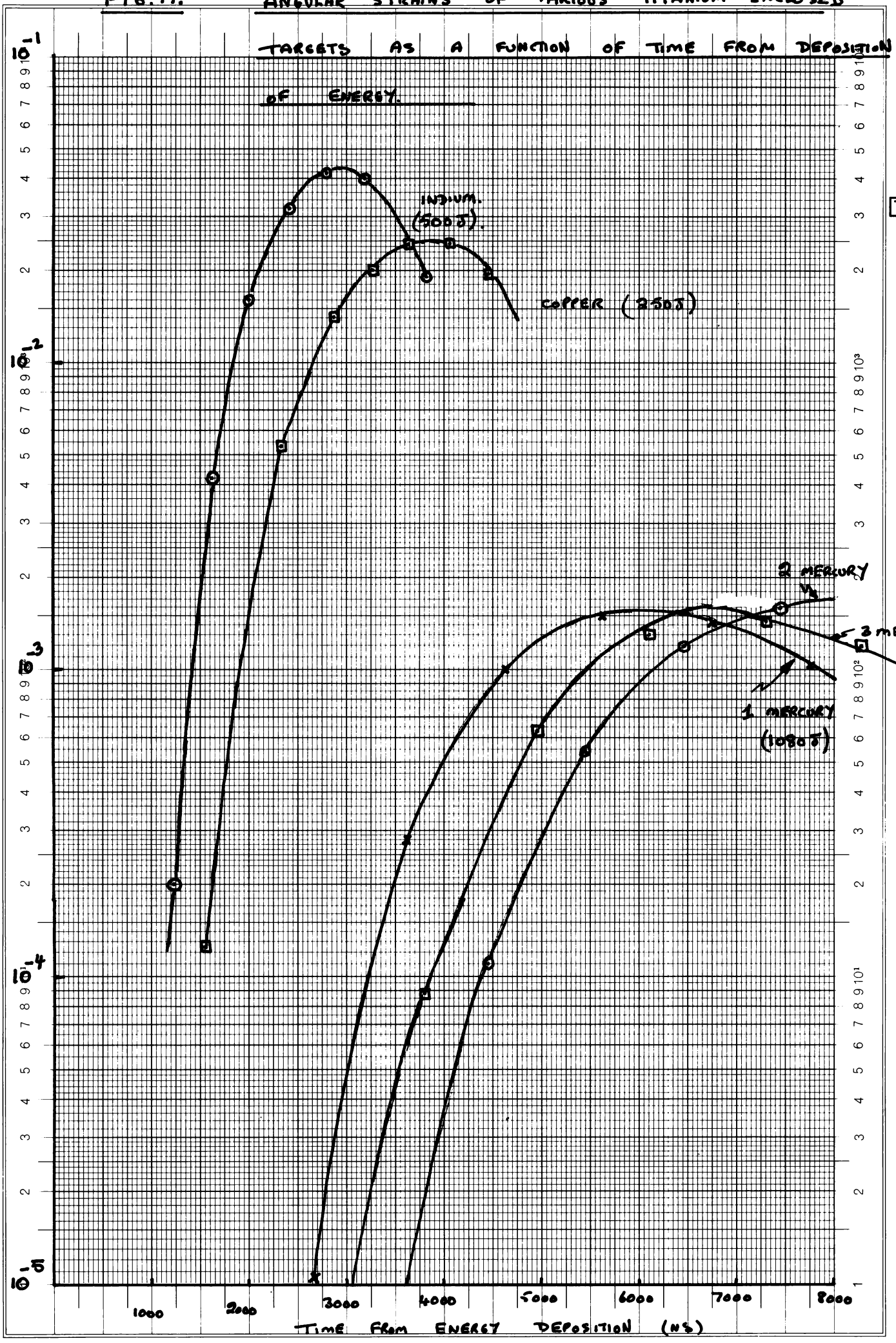

FIG. 18. TIME EVOLUTION OF RADIAL STRAIN IN CERAMIC. MERCURY TARGET.

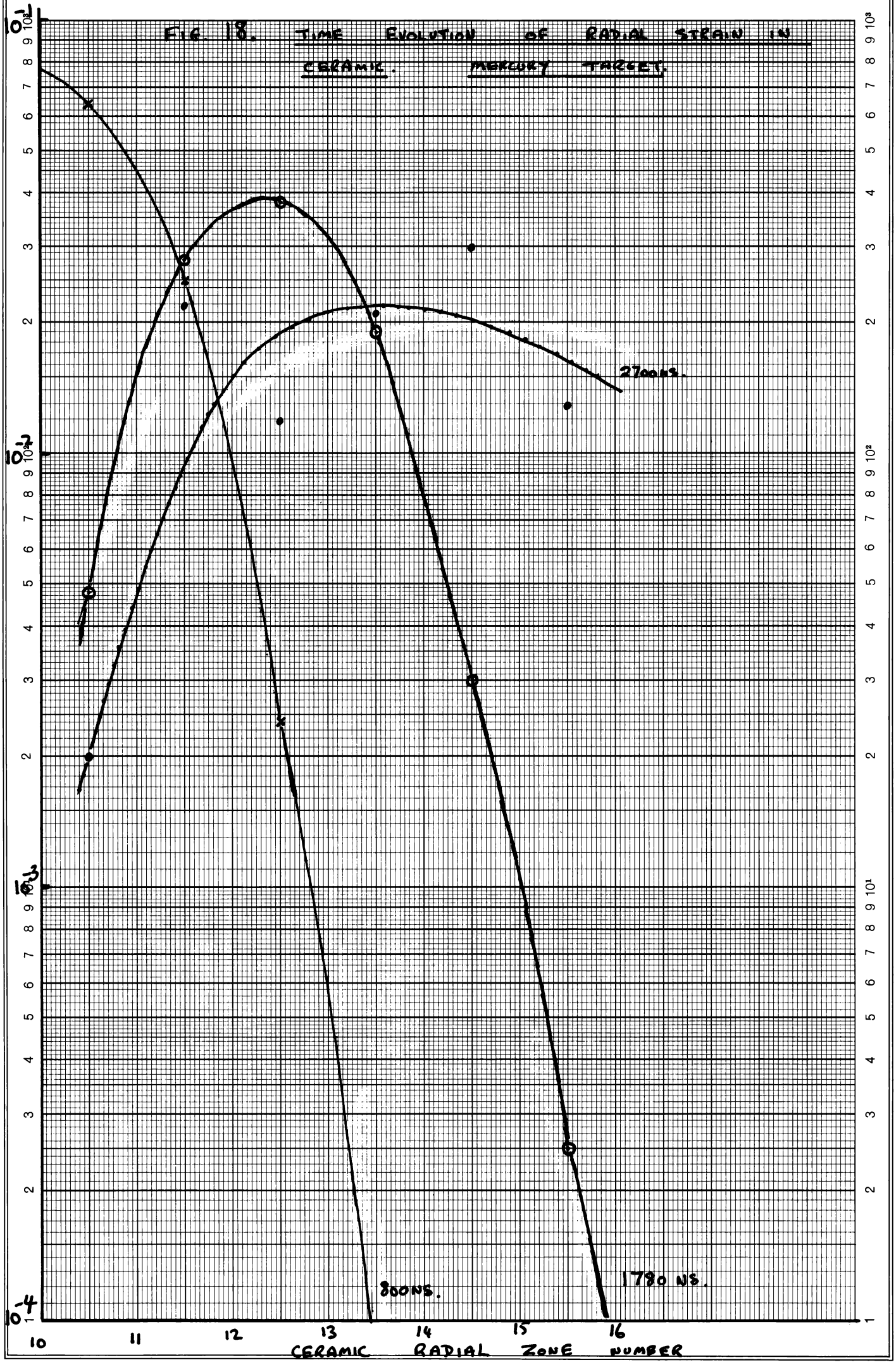

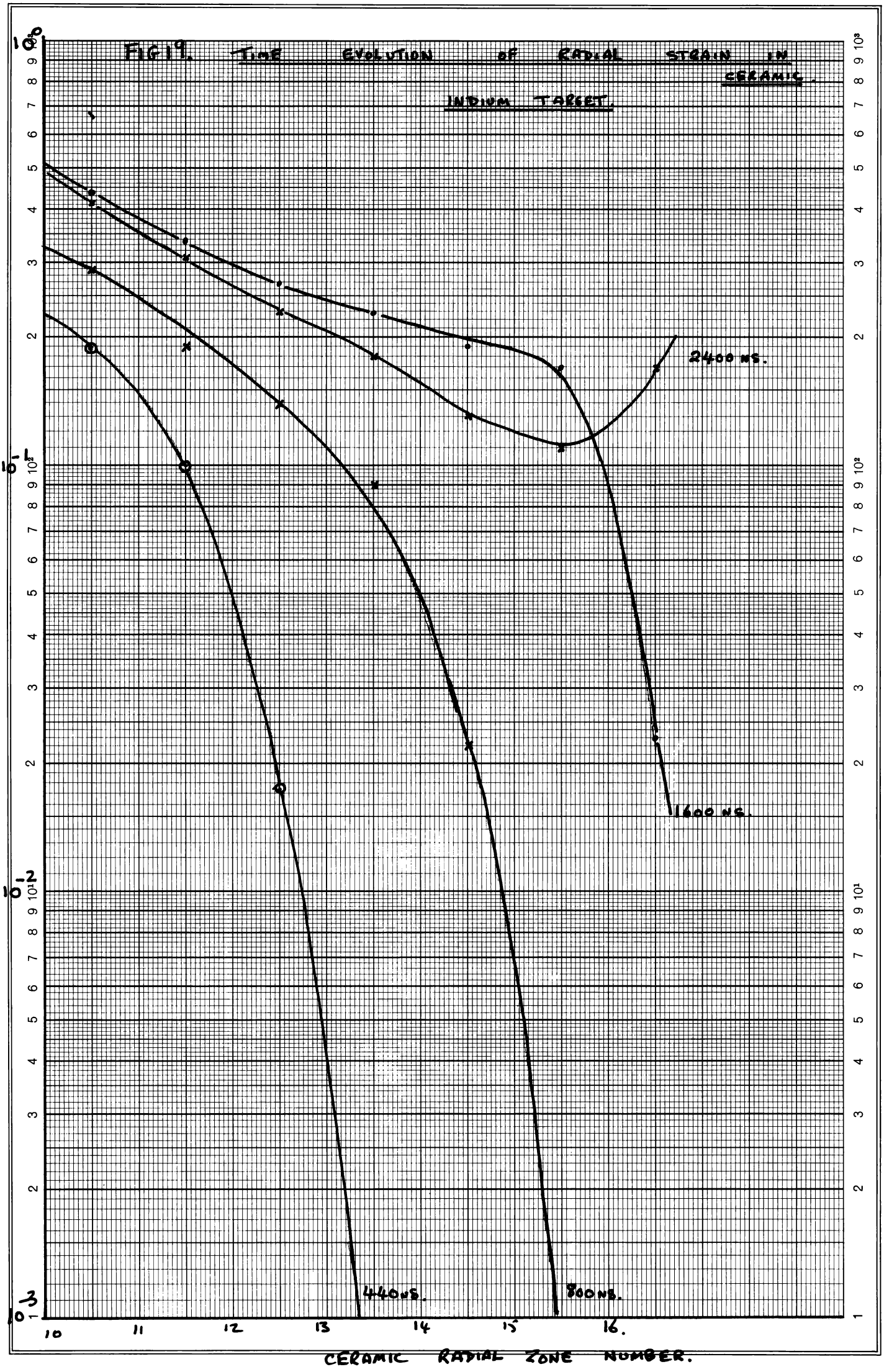

TABLE 1 POSITION OF PRESSURE WAVE FRONT AS A FUNCTION OF TIME

TIME ns.	RADIAL POSITION.
15	7·05 ± ·05
47	8·80 ± ·05
62	9·15 ± ·05
94	9·9 ± ·1
156	10·4 ± ·1
219	12·1 ± ·1
406.	15·7 ± ·1

(A) GRADIENT OF GRAPH = 2.4×10^{-2} radial zones m^{-1}

EACH RADIAL ZONE = 0,18 mm. = $1,8 \times 10^{-4}$ m.

$$\therefore A = \frac{2.4 \times 10^{-2} \times 1.8 \times 10^{-4}}{10^{-9}}$$

$$A = 2,4 \times 10^{3} \ m s^{-1}$$

PLOT 1. MESH PLOTS AS A FUNCTION OF TIME FROM ENERGY INPUT

SIMPLE MERCURY COLUMN. NO CERAMIC.

$E_0 = 1600$ J.

CYCLE NUMBER = 0
TIME (SEC) = 0.000000000

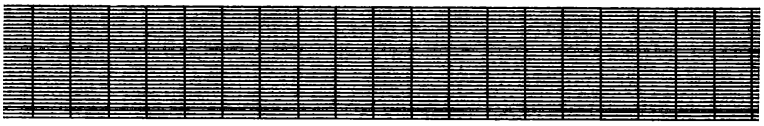

CYCLE NUMBER = 20
TIME (SEC) = 0.000000391

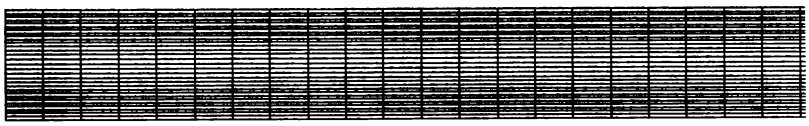

CYCLE NUMBER = 40
TIME (SEC) = 0.000000674

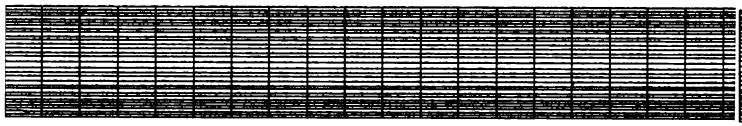

CYCLE NUMBER = 60
TIME (SEC) = 0.000000971

CYCLE NUMBER = 80
TIME (SEC) = 0.000001299

CYCLE NUMBER = 100
TIME (SEC) = 0.000001658

CYCLE NUMBER = 120
TIME (SEC) = 0.000001971

CYCLE NUMBER = 140
TIME (SEC) = 0.000002277

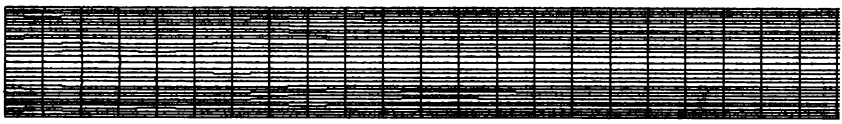

CYCLE NUMBER = 170
TIME (SEC) = 0.000002711

CYCLE NUMBER = 200
TIME (SEC) = 0.000003180

CYCLE NUMBER = 0
TIME (SEC) = 0.000000000

CYCLE NUMBER = 20
TIME (SEC) = 0.000000625

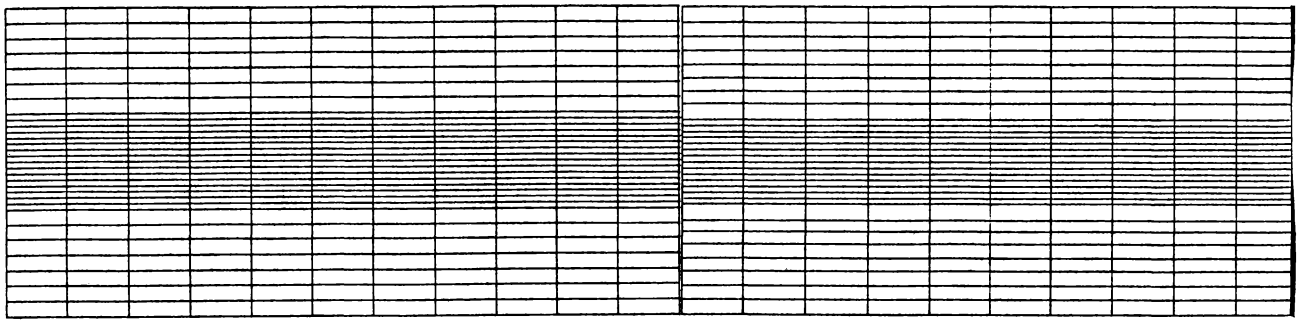

CYCLE NUMBER = 50
TIME (SEC) = 0.000001500

CYCLE NUMBER = 80
TIME (SEC) = 0.000002437

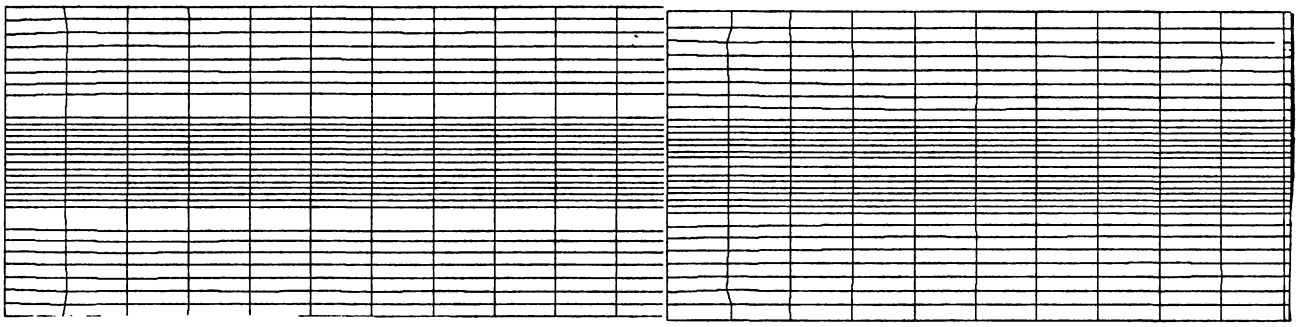

PLOT 2. MESH PLOTS AS A FUNCTION OF TIME FROM ENERGY INPUT

CYCLE NUMBER = 110
TIME (SEC) = 0.000003375

CYCLE NUMBER = 140
TIME (SEC) = 0.000004312

COPPER TARGET
$E_0 = 850$ J

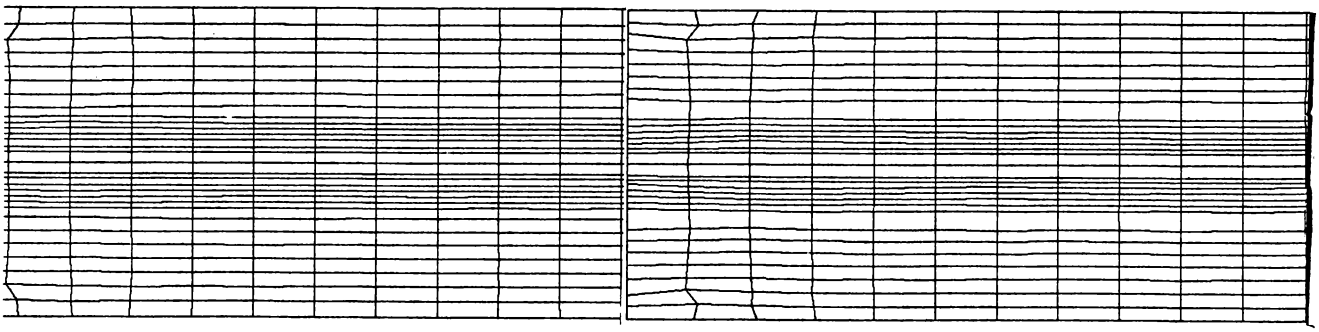

CYCLE NUMBER = 170
TIME (SEC) = 0.000005187

CYCLE NUMBER = 200
TIME (SEC) = 0.000006078

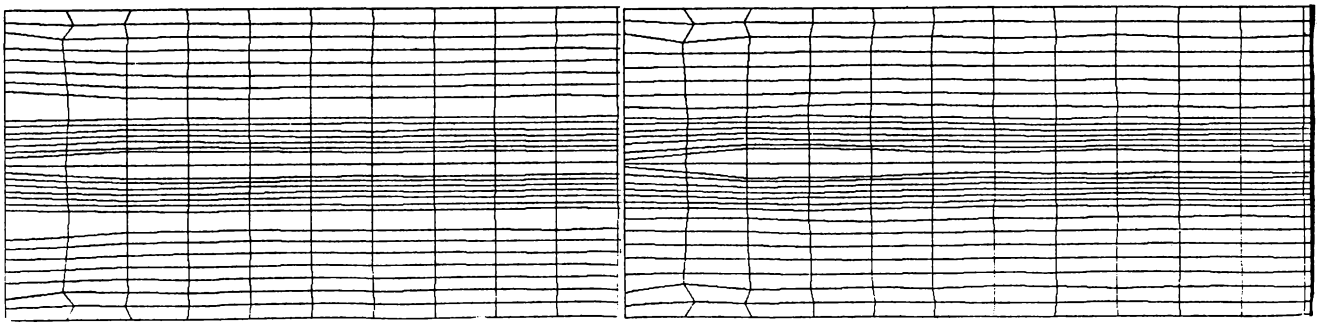

PLOT 3. DISTORTION OF TARGET MESH IN MERCURY. NON-UNIFORM ENERGY DEPOSITION.

CYCLE NUMBER = 0
TIME (SEC) = 0.000000000

CYCLE NUMBER = 30
TIME (SEC) = 0.000000969

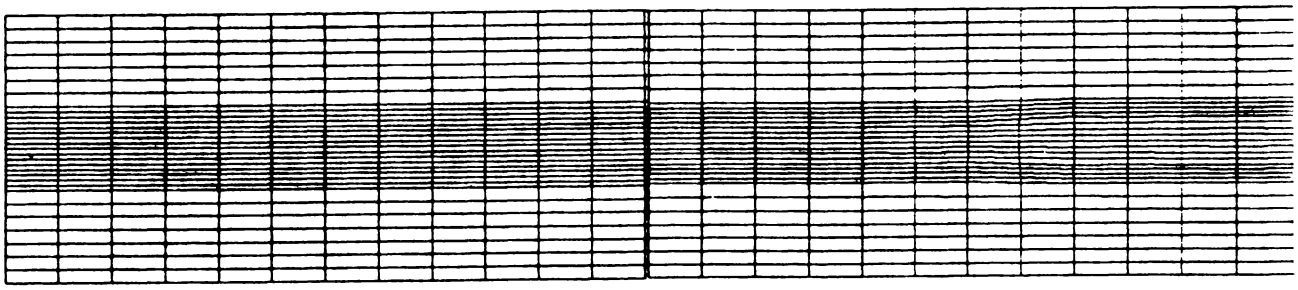

CYCLE NUMBER = 60
TIME (SEC) = 0.000001908

CYCLE NUMBER = 90
TIME (SEC) = 0.000002844

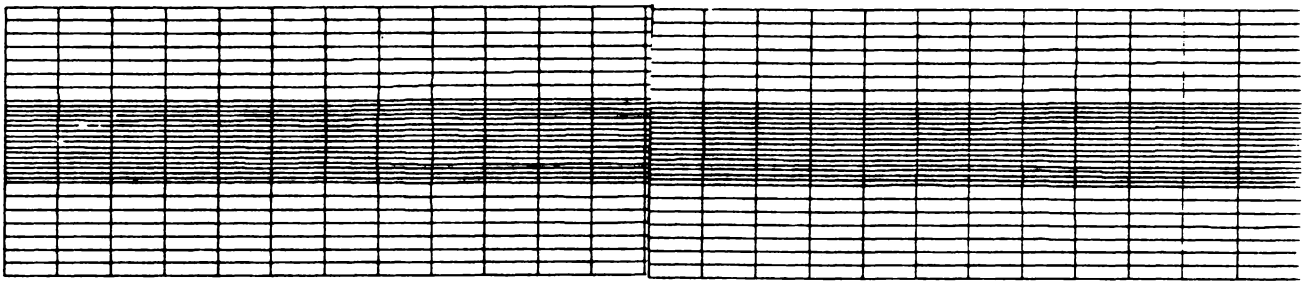

CYCLE NUMBER = 120
TIME (SEC) = 0.000003781

CYCLE NUMBER = 150
TIME (SEC) = 0.000004719

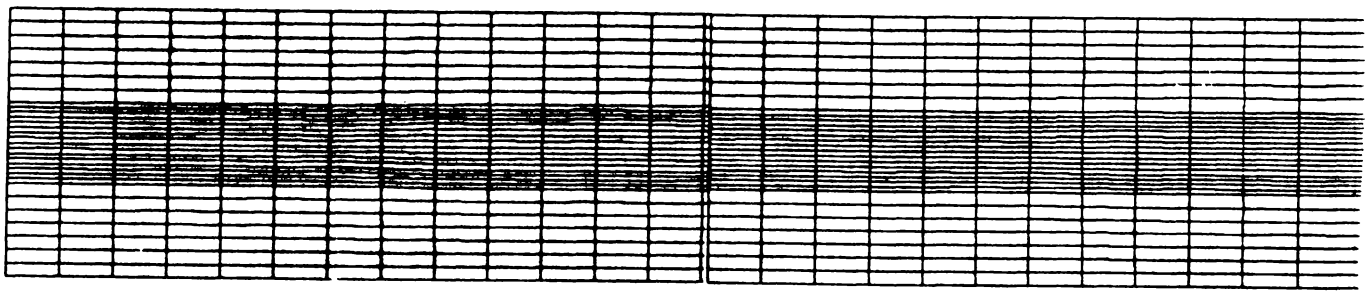

CYCLE NUMBER = 180
TIME (SEC) = 0.000005656

CYCLE NUMBER = 200
TIME (SEC) = 0.000006281

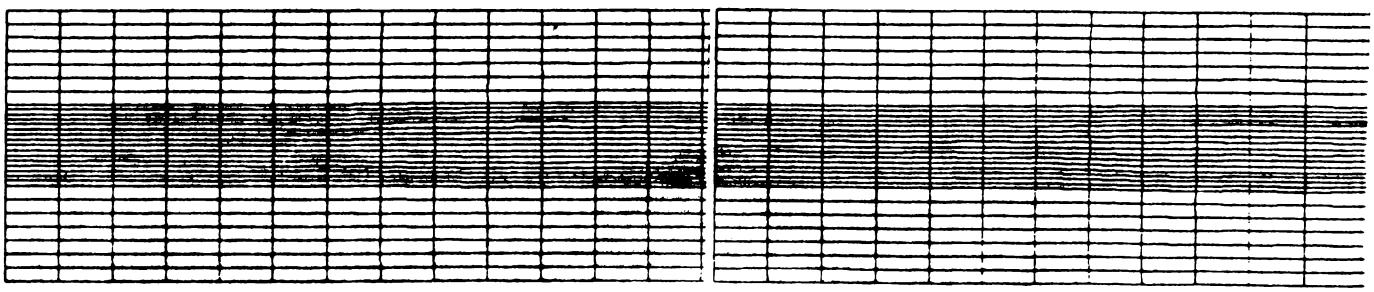

PLOT 4. DISTORTION OF TARGET MESH IN COPPER. NON UNIFORM ENERGY DEPOSITIO

CYCLE NUMBER = 0
TIME (SEC) = 0.000000000

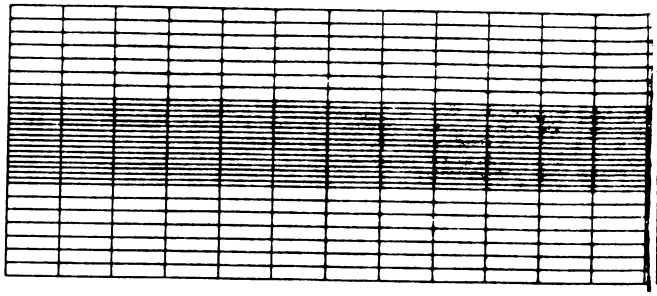

CYCLE NUMBER = 30
TIME (SEC) = 0.000000969

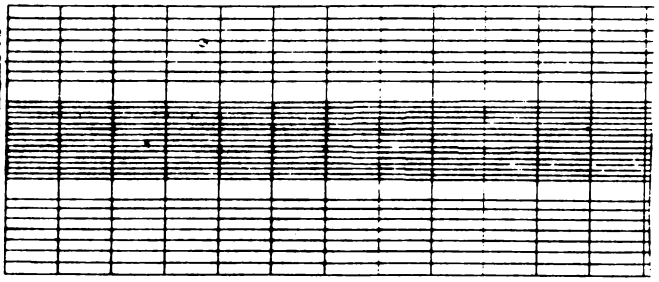

CYCLE NUMBER = 60
TIME (SEC) = 0.000001875

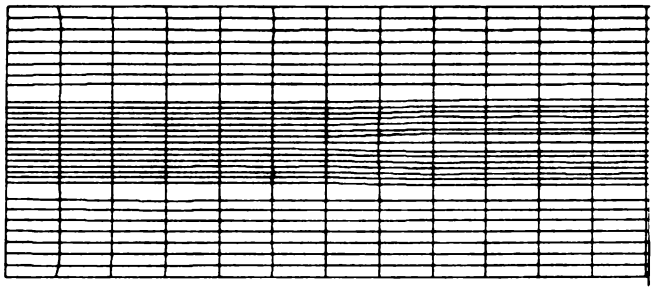

CYCLE NUMBER = 90
TIME (SEC) = 0.000002812

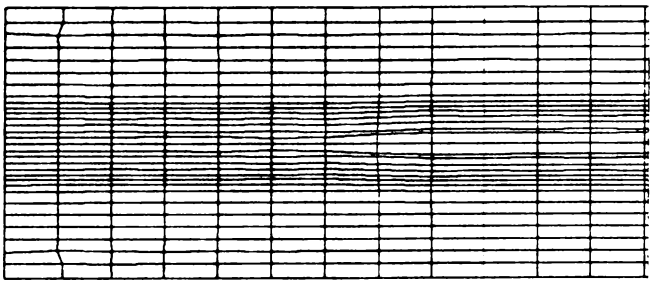

CYCLE NUMBER = 120
TIME (SEC) = 0.000003750

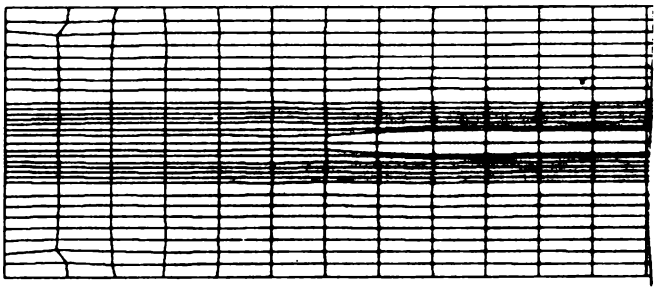

CYCLE NUMBER = 150
TIME (SEC) = 0.000004687

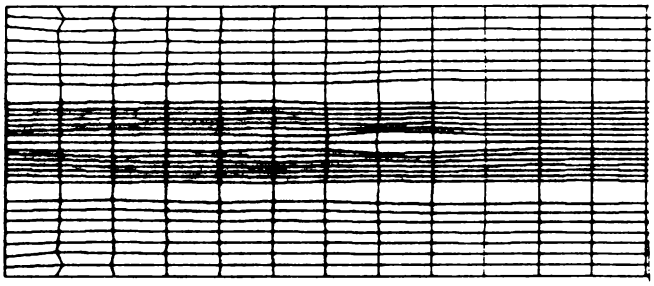

CYCLE NUMBER = 180
TIME (SEC) = 0.000005488

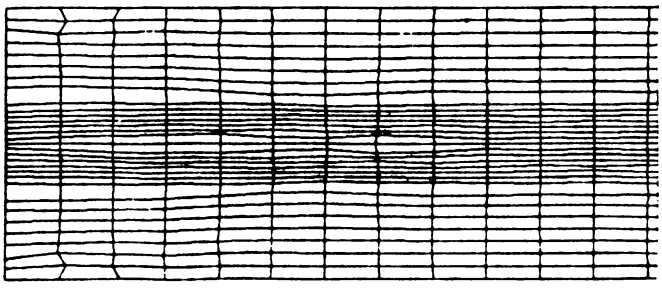

CYCLE NUMBER = 200
TIME (SEC) = 0.000006084